Computational Modeling of Oscillatory Motion with Finite Difference Time Domain Method

by

Yue Wu

A Report Submitted in Partial Fulfillment
of the Requirements for the Degree of

MASTER OF ENGINEERING

in the Electrical and Computer Engineering

University of Victoria

Abstracts

Finite Difference Time Domain (FDTD) method is a numerical analysis technique used in computational electromagnetics. Since it was proposed in 1966, FDTD method has become the fastest growing and the most popular method compared to other numerical solutions. Nowadays, using finite difference time domain method to model stationary object has been well established, there are several commercial and open-source FDTD solutions available on the market, which are excellent at modeling immobile devices. But little research has been performed to study the modeling of dynamic movements such as vibration and oscillation, which can be especially useful for studying deformations caused by forces like radiation pressure to better understand interactions between matter and electromagnetic waves. In this project, a two-dimensional FDTD model with an oscillating cylindrical rod was proposed and implemented. Using this model, the Raman scattering effect caused by an oscillation device was successfully observed. And a further investigation about the enhancement of Raman scattering when the incident frequency is near a whisper gallery mode resonance was performed. A minimal resonance shift caused by the oscillatory motion was also observed.

Table of Contents

1. Introduction

Since Maxwell established the governing equations for electromagnetic fields in 1873, electromagnetic theory and related researches have been over a hundred years. At present, the theory of electromagnetism has been widely applied in various fields like radio propagation, optical communication, antenna design, optical imaging, spectroscopy and so on. Propagation of electromagnetic fields in real environments can be very complicated, such as scattering from microscopic structures, radiation of complex antennas, propagation in waveguides, etc. With so many different applications, generalized computational models become increasingly important to give more insights on experiments and to verify experimental data with simulations. Many meaningful numerical solutions to Maxwell's equations have been proposed such as method of moments (MOM), finite element method (FEM), and finite difference time domain method (FDTD) etc., of which FDTD is becoming the fastest growing and the most popular method in use today. Nowadays signal scattering from a stationary object can be well simulated using FDTD method. As interests grow in understanding how matter interacts with electromagnetic waves, the analysis of the electromagnetic field around dynamic bodies also has received great interests. But few studies have used FDTD methods to study the modeling of dynamic motion such as vibration and oscillation, which can be especially useful for microscopic deformations caused by forces like radiation pressure.

The purpose of this project is to develop a model to simulate two-dimensional harmonic oscillation with finite difference time domain method, a custom FDTD program was implemented since no commercially available FDTD solvers provide tools to integrate the necessary modifications required for this task. This report is organized as follows: First, a review of literature that incorporates dynamic systems with numerical models is presented

in Section 2. In Section 3, a compressive review of FDTD method and its formulation is discussed, the corresponding code will be available in the appendix. Next in Section 4, a brief introduction of Raman scattering effect which is the main phenomenon could be observed with an oscillating object was presented. The methodology to incorporate an oscillating cylinder in our FDTD algorithm is also outlined. Then in Section 5, some simulation results based on the developed model are presented. And finally, Section 6 will be devoted to concluding remarks and a discussion of future works.

2. Background Literature

Although there is no conclusive numerical model yet, radiation pressure is widely considered to be the connection between electromagnetic and mechanical systems. A simulative experiment done by Max Waddell and Kenneth Chau [1] tried to incorporate different sets of electrodynamic postulates to model radiation pressure. In their research, they implemented electromagnetic and mechanical systems separately with FDTD to simulate the electromagnetic fields, then compute power, energy, stress, and momentum from the results based on different postulates and use them to simulate the kinetic moment with Newtonian dynamics. However, in their simulations, they assume that electromagnetic wave causes negligible displacement of the material, so the mechanical system was reduced to a center of mass analysis. This would not be a valid assumption for small particles and molecules since they will be oscillating under electromagnetic radiation. As demonstrated by Mihiretie, in their experiments [2,3] they observe ellipsoidal dielectric particles with higher refractive indices compared to the surrounding fluid, trapped around the laser beam and constantly vibrating, rotating, and oscillating. But despite observing the rotation and oscillation, their simulative analysis also only considers the spatial vibration and ignore the other two.

The reason they ignore oscillations is due in part to the fact that there are currently no established methods to model vibrating and oscillating object with electromagnetic fields. A few pieces of literature exist with oscillation been implemented in simulation techniques other than FDTD method, but these implementations have some major compromises. As a time-domain method, FDTD is inherently a better and more intuitive way to handle dynamic systems. To incorporate complex motion, such as oscillation, we first need to look

back to the evolution of modeling dynamic objects with finite difference time domain method.

It starts with modeling time-varying medium using FDTD method, the term time-varying means the property of the medium can be altered as a function of time independent of the electromagnetic field values. The theoretical studies of time-varying medium often found that the solutions of Maxwell's equations are extremely difficult to obtain in analytical forms, and the solutions obtained can only be applied to idealized problems. Taylor, Lam and Shumpert [4] were the first to prove this can be solved by FDTD method. In particular, they used FDTD algorithm to exam the electromagnetic pulse scattered from a cylindrical rod inside a cylindrical waveguide, the conductivity of the cylindrical rod was assumed to be linearly increasing as a function of time, but the permittivity was kept constant. Harfoush [5] applied FDTD solutions to analyzes electromagnetic wave penetrated and scattered from a material with its conductivity time-varying sinusoidaly. Comparisons of the FDTD solutions to their analytical results were excellent. Liu [6] have presented literature dedicated to investigating the stability of FDTD method for modeling time-varying permittivity by comparing the simulation results with previous results obtained using theoretical approaches in other works. One simulation was done for plane wave interaction with a dielectric slab that has sinusoidal time-varying permittivity, and the other was for a microstrip patch antenna on a substrate with a sinusoidal time-varying permittivity. The stability of the FDTD solution in their case proved to be very promising. The author also mentioned that by changing the permittivity sufficiently slowly with respect to the frequency of the incoming wave, the permittivity variation can be considered time-invariant, and the result becomes more accurate.

After proving that the problem of time-varying properties can be solved using finite difference time domain method, several numerical implantations have been proposed to model uniform translational motions with the FDTD method. The first time FDTD was ever used in modeling electromagnetic wave scattered by moving object was done by the research group of Allen Taflove. In their paper [7], Harfoush introduced a numerical approach to deal with the electromagnetic wave scattering properties for moving or vibrating objects. The movement of the object was realized by relativistic boundary condition. However, the relativistic boundary condition was only adopted for perfect conducting mirrors, that is objects only receding the incident wave without transmission or refraction. Also, the vibration in his paper was merely two translational motion in opposite directions since the mirror was not deformed. The author also mentioned that by considering a sufficiently small velocity, the ratio between the object's velocity and speed of light v/c could then be ignored. Thus, the formulation of the relativistic boundary condition became a total reflection function with the field reflected by the boundaries being doubled. Which indicate that the boundary condition is not as important in low velocities as in high-speed scenarios.

Recently Inman et al. [8] reported a method to realize a constant speed movement by using dielectric approximation and intermedia-step field movement. On the forward-boundary of the moving object, dielectric coefficients are modified at each step until they possess the properties of an inside cell. Likewise, on the back-boundary cell, they are modified until they become free space properties. After the coefficients are modified, the fields inside and outside the boundary are split in two as total-field and object-field. The total-field outside the boundary is a summation of the background field without the object's present and the

object-field that was assumed as a portion of the field that exists only within the moving object. The ratio of the object-field versus the total-fields was assumed to be governed by the permittivity of the medium. Then the object-field was also considered to be spatially shifted, therefore, a correction term was calculated with a Lagrange approximation in the direction of the movement, however, this correction term is only feasible for objects moving in one direction. And won't be necessary at all if the movement is sufficiently slow compared to the speed of the light, renders the shift insignificant. Inman's method relied heavily on precomputed lookup tables since the entire coefficient approximation and Lagrange approximation was precomputed which can be easily done in one-dimensional cases and two-dimensional cases with only one directional movement but become dramatically more difficult to generalize for off-axis translational motion or vibrations in two dimensions.

A more recent technique proposed by Hiroshi Iwamatsu [9] combines Lorentz transformations with FDTD method was dedicated to analyzing interactions with high velocities close to the speed of light. The moving devices were modeled on a secondary sub-grid and can be considered static in perspective of the sub-grid, but the sub-grid was moving relative to the main grid. Since the object is stationary in the perspective of its own grid, regular FDTD simulations can be performed separately in each grid, then the fields need to be interpolated between two grids with Lorentz transformations. Considering two set of grids need to be simulated at the same time, this approach is incredibly computationally demanding compared to normal FDTD algorithms.

In general, these are the three main methods for molding moving bodies with the FDTD method currently proposed. But the interests of these methods were mainly focused on

high-speed moving bodies, and most of the techniques could not be transferred to model vibration and oscillation. Currently, there is no meaningful literature tried to incorporate vibration and oscillation with FDTD methods alone. Although few attempts have been made to simulate them with other numerical methods.

Murray [10] introduce an analytical theory to calculate the polarizability of oscillating nanoparticles. The vibrational motion was described by spherical harmonic functions. Since his entire method was built on a Spherical coordinate system with no time domain element, it would be difficult to adopt it in FDTD. The author also states that "FDTD cannot handle very small changes in the object since it must use a coarse grid of spatial points" which touches on one major drawback of the technique, that is small shapes are difficult to be accurately represented by rectangular grids. This can be solved by either a higher resolution or alternative grid systems like hexagonal grids or curvilinear grids, etc. However, either increasing the resolution or using alternative grid systems will also result in requiring considerably more computational resources. It is worth noting that Murray also points out the permittivity of the ellipsoid in his method needs to be smoothed. But different to Inman's approach by smooth the permittivity only on the boundary over time, he smoothed the permittivity over a short distance near the surface, which alters the effective radius of the nanoparticle. A drawback that can be easily avoided with time domain methods.

To understand how waves scattered from metal nanoparticles respond to vibrations, Ahmed used FDTD calculations only for the optical response in his paper [11]. The structural changes were modeled by solving the Navier equation with the continuity of stress and displacement at the boundary using the finite element method. In their case, the vibration

of a two-dimensional nanowire was molded by a cylindrical nanorod with fixed width. The deformation was done by changing the length of the rod, which somehow represents an oscillation ellipse. But since the width is fixed, the vibration is essentially two translational motion in opposite directions, similar to what Harfoush did with his mirror vibrations. The boundary condition was not addressed at all in this paper, however, the vibrational speed described in the paper was considerably slow compared to the speed of light. Thus, giving us more reason to believe that the boundary condition may not be as important for simulations with ultra-slow velocities.

Methods to incorporate vibrations were also implemented in cavity optomechanical crystals analysis by research groups of Vahala and Painter in recent years. As showcased by Eichenfield [12], they use a Finite element method to compute both electromagnetic and mechanical systems, the mechanical displacement profile is defined to describe the perpendicular displacements of volume elements. Optical and mechanical mode volumes are defined by electric field and mechanical displacement profile to gauge the strength of light-matter interactions. Then vibrations were introduced via a variable effective length coefficient calculated by optical, mechanical mode volumes and electric field values, based on a first-order perturbation theory of Maxwell's equations that was described in [13]. This approach is an elegant way to incorporate deformation, but also has its own limitations. For example, the perturbation theory only possesses the first-order accuracy and usually does not handle nonlinear effects well.

3. Finite Difference Time Domain Method

This section presents a review and formulation of the finite difference time domain methods as well as formulations of different techniques relate to the FDTD that is used in this project, including perfectly matched layer boundary conditions, Courant-Friedrichs-Lewy stability conditions, Gaussian pulses, plane wave excitations and total-field/scattered-field techniques, etc.

3.1. Maxwell's Equations

In general, electric and magnetic fields can be represented by vector quantities that have both magnitude and direction. The behavior of electric and magnetic fields generated by electric charges or a flow of electric current are governed by physical laws known as Maxwell's equations which can be expressed in a set of partial differential equations as:

Gauss's law: $$\nabla \bullet \vec{D} = \rho \tag{3.1}$$

$$\nabla \bullet \vec{B} = 0 \tag{3.2}$$

Faraday's law: $$\nabla \times \vec{E} = -\frac{\partial \vec{B}}{\partial t} \tag{3.3}$$

Ampere's law: $$\nabla \times \vec{H} = \frac{\partial \vec{D}}{\partial t} + \vec{J} \tag{3.4}$$

Where $\vec{D}$ is electric flux density, ρ is electric charge density, $\vec{B}$ is magnetic flux density, $\vec{E}$ is electric field intensity, $\vec{H}$ is magnetic field intensity, and $\vec{J}$ is electric current density. The response between $\vec{D}$ and $\vec{E}$, as well as $\vec{B}$ and $\vec{H}$ are specified through constitutive relations, for linear materials, they are:

$$\vec{D} = [\varepsilon]\vec{E} = \varepsilon_0 [\varepsilon_r]\vec{E} \tag{3.5}$$

$$\vec{B} = [\mu]\vec{H} = \mu_0 [\mu_r]\vec{H} \tag{3.6}$$

Where $[\varepsilon]$ is the permittivity of the material that equals to free-space permittivity constant ε_0 multiply by the relative permittivity tensor $[\varepsilon_r]$. Similarly, the permeability of the material $[\mu]$ is the product of free-space permeability μ_0 and relative permeability $[\mu_r]$. Electric current density $\vec{J}$ can be estimated with conductivity $[\sigma]$ through Ohm's law:

$$\vec{J} = [\sigma]\vec{E} \tag{3.7}$$

In linear, non-dispersive materials, Maxwell's equations can be represented with only electric and magnetic fields as:

$$\nabla \times \vec{E} = \mu_0 [\mu_r] \frac{\partial \vec{H}}{\partial t} \tag{3.8}$$

$$\nabla \times \vec{H} = \varepsilon_0 [\varepsilon_r] \frac{\partial \vec{E}}{\partial t} + [\sigma]\vec{E} \tag{3.9}$$

3.2. Yee's Algorithm

In 1966 Kane S. Yee [14] proposed the Finite Difference Time Domain algorithm which is a numerical solution of Maxwell's equations. By applying a set of central-difference approximations, the spatial and temporal derivatives appearing in Maxwell's equations can be estimated with second-order accuracy. Consider a function f, its Taylor-series expansions at points $x_0 \pm \frac{\delta}{2}$ are:

$$f\left(x_0 + \frac{\delta}{2}\right) = f(x_0) + \frac{\delta}{2} f'(x_0) + \frac{1}{2!}\left(\frac{\delta}{2}\right)^2 f^{(2)}(x_0) + \frac{1}{3!}\left(\frac{\delta}{2}\right)^3 f^{(3)}(x_0) + \ldots. \tag{3.10}$$

$$f\left(x_0 - \frac{\delta}{2}\right) = f(x_0) - \frac{\delta}{2} f'(x_0) + \frac{1}{2!}\left(\frac{\delta}{2}\right)^2 f^{(2)}(x_0) - \frac{1}{3!}\left(\frac{\delta}{2}\right)^3 f^{(3)}(x_0) + \ldots \tag{3.11}$$

Subtracting (3.11) from (3.10) then divided by δ yields:

$$\frac{f\left(x_0+\frac{\delta}{2}\right)-f\left(x_0-\frac{\delta}{2}\right)}{\delta}=f'(x_0)+\frac{1}{3!}\left(\frac{\delta}{2}\right)^2 f^{(3)}(x_0)+\cdots \tag{3.12}$$

Therefore, the left-hand side of the equation equals to the derivative of f at x_0 plus $O(\delta^2)$. Provided δ is sufficiently small, a reasonable second-order approximation for an arbitrary point x_0 could be given by:

$$\left.\frac{\partial f(x)}{\partial x}\right|_{x=x_0} \approx \frac{f\left(x_0+\frac{\delta}{2}\right)-f\left(x_0-\frac{\delta}{2}\right)}{\delta} \tag{3.13}$$

Note that the approximation is not sampled at x_0, but at its neighboring positions $x_0 \pm \delta/2$ instead. To accommodate this, Yee also proposed a simple yet elegant rectangular grid scheme that staggers the electric and magnetic fields both spatially and temporally. This scheme now known as Yee grid has proven to be very robust and become the core of modern FDTD algorithms.

3.3. Yee Grid

Consider a three-dimensional rectangular grid, each grid cell has the length of Δx, Δy and Δz along each axis, and a time difference of Δt to its adjacent cells. A notation $f^{i,j,k}(n)$ can express any cell in the grid with:

$$(i, j, k) = (i \cdot \Delta x,\ j \cdot \Delta y, k \cdot \Delta z) \tag{3.14}$$

And:
$$n = (n \cdot \Delta t) \tag{3.15}$$

Within this grid system, vector components of the electric field are projected parallel to the edge of the cells and are sampled at the center of each edge. Vector components of the magnetic field are projected normal to the faces of the cell and are sampled at the center of each face as illustrated in Figure.1a. Note that each $\vec{E}$ component and its surrounding $\vec{H}$

components have a half spatial difference as well as a half temporal difference, vice versa, each $\vec{H}$ component with its surrounding $\vec{E}$ components also has a half spatial and temporal differences demonstrated in Figure.1b-Figure.1c.

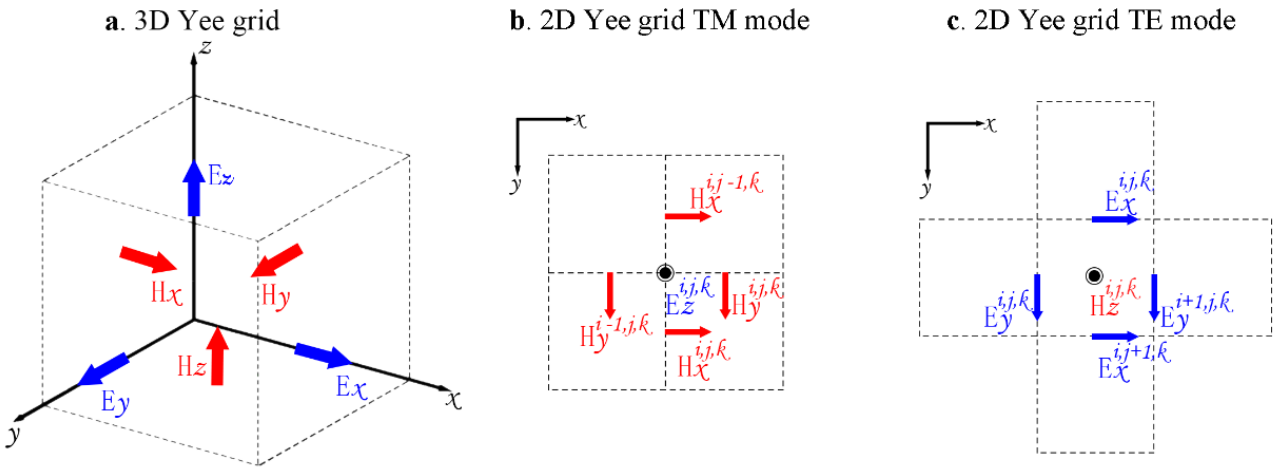

Figure 1. a. standard 3-D Yee cell with perspective of the spatial locations of $\vec{E}$ and $\vec{H}$ components. b. 2-D Yee cells in transverse-magnetic (TM) mode with perspective of positions between Ez component and $\vec{H}$ components. c. 2-D Yee cells in transverse-electric (TE) mode with perspective of positions between Hz component and $\vec{E}$ components.

3.4 Update Equation for $\nabla \times \vec{E}$ and $\nabla \times \vec{H}$

This grid system works perfectly with our central-difference approximations and provides essential pieces for formulating the curl operations in Maxwell's equations which can be expressed as:

$$\nabla \times \vec{E} = \left(\frac{\partial E_z}{\partial y} - \frac{\partial E_y}{\partial z}\right)\hat{\mathbf{x}} + \left(\frac{\partial E_x}{\partial z} - \frac{\partial E_z}{\partial x}\right)\hat{\mathbf{y}} + \left(\frac{\partial E_y}{\partial x} - \frac{\partial E_x}{\partial y}\right)\hat{\mathbf{z}} \tag{3.16}$$

$$\nabla \times \vec{H} = \left(\frac{\partial H_z}{\partial y} - \frac{\partial H_y}{\partial z}\right)\hat{\mathbf{x}} + \left(\frac{\partial H_x}{\partial z} - \frac{\partial H_z}{\partial x}\right)\hat{\mathbf{y}} + \left(\frac{\partial H_y}{\partial x} - \frac{\partial H_x}{\partial y}\right)\hat{\mathbf{z}} \tag{3.17}$$

For purpose of this project, the formulations will be reduced to two-dimensional TM mode via assuming partial derivatives of fields with respect to z detention equal to zero. And only preserve the z component of the electric field, x and y components of the magnetic field. The simulative results of the TM and TE mode have proven to be identical. Also CE_x

and CE_y is denoted as the curl of $\vec{E}$ in x, y directions, CH_z as the curl of $\vec{H}$ in z direction. Using spatial central-difference approximations for each derivative in the curl operations, for point (i, j) at time t the vector expansion of the curl operations becomes:

$$CE_x^{i,j}(t) = \frac{\partial E_z}{\partial y} - \frac{\partial E_y}{\partial z} = \frac{E_z^{i,j+1}(t) - E_z^{i,j}(t)}{\Delta y} - 0 \tag{3.18}$$

$$CE_y^{i,j}(t) = \frac{\partial E_x}{\partial z} - \frac{\partial E_z}{\partial x} = 0 - \frac{E_z^{i+1,j}(t) - E_z^{i,j}(t)}{\Delta x} \tag{3.19}$$

$$CH_z^{i,j}(t) = \frac{\partial H_y}{\partial x} - \frac{\partial H_x}{\partial y} = \frac{H_y^{i,j}(t) - H_y^{i-1,j}(t)}{\Delta x} - \frac{H_x^{i,j}(t) - H_x^{i,j-1}(t)}{\Delta y} \tag{3.20}$$

Note that $CE_x^{i,j}$ exists at the same spatial position as $H_x^{i,j}$ which is located at $E_z^{i,j+1/2}$, same goes for $CE_y^{i,j}$ exists at $E_z^{i+1/2,j}$ and $CH_z^{i,j}$ locate at the same position as $H_y^{i,j-1/2}$ and $H_x^{i-1/2,j}$, such being the case, x_0 in Eq. (3.12) correspond to $j + 1/2$, $i + 1/2$, $i - 1/2$, $j - 1/2$ in Eq. (3.18-3.19) respectively.

Before proceeding to the right side of Maxwell's equations in Eq. (3.8-3.9), the boundary conditions should be discussed first, since after implementing loss into the boundary, some artificial property will be added that changes the formulation.

3.5 Absorbing Boundary Conditions and Perfectly Matched Layer (PML)

When running FDTD simulations, a boundary must be artificially added that will terminate the grid via effectively absorbing any electromagnetic field that travels beyond the problem domain. Such a boundary is referred to as the absorbing boundary condition (ABC). Traditional ABC methods are extremely computationally demanding and still reflect a noticeable amount of energy back to the computational domain [15]. The 90s saw the emergence of absorbing media ABCs, including some powerful methods as Berenger's

original perfectly matched layer (PML) [16] and later a more efficient and more popular uniaxial PML (UPML) [17] [18]. The property of the PML region is selected such that waves incident upon the PML region do not reflect at the interface, meanwhile exponentially decaying inside the PML region.

The PML region is considered to be composed of an anisotropic material that has complex diagonal permittivity and permeability tensors in the form of:

$$\begin{bmatrix} \mu_x + \frac{\sigma_x}{j\omega} & 0 & 0 \\ 0 & \mu_y + \frac{\sigma_y}{j\omega} & 0 \\ 0 & 0 & \mu_z + \frac{\sigma_z}{j\omega} \end{bmatrix} = [\mu_r] = \frac{[\mu]}{\mu_0} \tag{3.21}$$

$$\begin{bmatrix} \varepsilon_x + \frac{\sigma_x}{j\omega} & 0 & 0 \\ 0 & \varepsilon_y + \frac{\sigma_y}{j\omega} & 0 \\ 0 & 0 & \varepsilon_z + \frac{\sigma_z}{j\omega} \end{bmatrix} = [\varepsilon_r] = \frac{[\varepsilon]}{\varepsilon_0} \tag{3.22}$$

Where $\varepsilon_{x,y,z}$, $\mu_{x,y,z}$, $\sigma_{x,y,z}$ are properties exclusive to the PML region. The loss is incorporated by a fictitious conductivity mimicking loss caused by real conductivity. In order to incorporate loss without introducing additional reflection from the change of impedance, the impedance of the PML required to be matched to free space:

$$\eta_r = \sqrt{\frac{\mu}{\varepsilon}} = \sqrt{\frac{\mu_0}{\varepsilon_0}} \tag{3.23}$$

Which implies that $[\varepsilon_r] = [\mu_r]$, thus our diagonal tensors in Eq. (3.21-3.32) can be expressed in the same form as:

$$[S] = \frac{[\mu]}{\mu_0} = \frac{[\varepsilon]}{\varepsilon_0} = \begin{bmatrix} a & 0 & 0 \\ 0 & b & 0 \\ 0 & 0 & c \end{bmatrix} \tag{3.24}$$

In their paper Sacks et al. [18] showcase that the refraction and reflection can be manipulated through the choice of a, b and c. Consider the problem of a wave entering the PML in z direction represented in Figure.2, according to [19] the Snell's law for diagonally anisotropic media can be expressed in the form:

$$\sin\theta_i = \sin\theta_r \tag{3.25}$$

$$\sin\theta_i = \sqrt{bc}\sin\theta_t \tag{3.26}$$

Reflection coefficients for the TM and TE modes r_{TM} and r_{TE} in Fresnel equations can be written as:

$$r_{TM} = \frac{\sqrt{a}\cos\theta_i - \sqrt{b}\cos\theta_t}{\sqrt{a}\cos\theta_i + \sqrt{b}\cos\theta_t} \tag{3.27}$$

$$r_{TE} = \frac{\sqrt{b}\cos\theta_t - \sqrt{a}\cos\theta_i}{\sqrt{a}\cos\theta_i + \sqrt{b}\cos\theta_t} \tag{3.28}$$

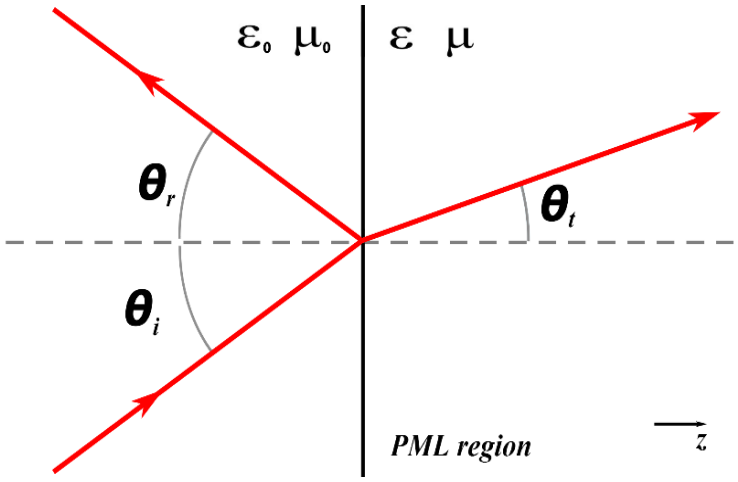

Figure 2. Reflection and refraction represented when wave inter PML interface on a z plane, θ_i is the angle of incident wave, θ_r is the angle of reflection, θ_t is the angle of refraction.

By imposing the condition $bc = 1$, the refraction will be removed by forcing $\theta_i = \theta_t$, $\cos\theta_i$ and $\cos\theta_t$ can also be canceled out, which indicates the reflection will no longer be a function of incident and transmission angles. By further imposing the condition $a = b$, both reflection coefficients must be zero. This property is completely independent of the incidence angle, polarization or incident frequency. Therefore, for any wave traveling in z direction, our PML tensor should have $a = b = c^{-1}$, which makes the PML property uniaxial anisotropic. And the diagonal tensor $[S]$ in z direction can be written as:

$$[S_z] = \begin{bmatrix} s_z & 0 & 0 \\ 0 & s_z & 0 \\ 0 & 0 & s_z^{-1} \end{bmatrix} \tag{3.29}$$

Similar to wave entering in the z direction, for waves traveling in x and y directions should have $a^{-1} = b = c$ and $a = b^{-1} = c$ respectively. Combining three x, y, z directional tensors into a single tensor quantity results in:

$$[S] = [S_x][S_y][S_z] = \begin{bmatrix} s_x^{-1}s_y s_z & 0 & 0 \\ 0 & s_x s_y^{-1} s_z & 0 \\ 0 & 0 & s_x s_y s_z^{-1} \end{bmatrix} \tag{3.30}$$

Where $s_{x,y,z} = 1 + \sigma_{x,y,z}/j\omega\varepsilon_0$, which is the most popular choices for implementing loss in many PML implementations. It's important to note that since $s_{x,y,z}$ only have physical properties inside the PML region, $[S]$ should be an identity tensor in normal computational domain i.e. $\sigma_{x,y,z} = 0$ outside the PML region, meanwhile gradually increased within the PML. The common method to achieve this is polynomial grading as:

$$\sigma_{x,y,z}(n) = \sigma_{max}\left(\frac{n}{d}\right)^m \tag{3.31}$$

Where n is the depth within the PML region, d is the total depth of PML, σ_{max} is a maximum conductivity when $n = d$. For many FDTD simulations, $m = 3{\sim}4$ has found to be optimal, and an optimal choice for maximum conductivity can be expressed as [15] [17]:

$$\sigma_{opt} \approx \frac{m+1}{150\pi\Delta(x,y,z)} \tag{3.32}$$

3.6 Update Equation with PML

The general time-harmonic form of Faraday's and Ampere's law in Eq. (3.8-3.9) can be written as:

$$\nabla \times \vec{E}(\omega) = -j\omega[\mu]\vec{H}(\omega) \tag{3.33}$$

$$\nabla \times \vec{H}(\omega) = j\omega[\varepsilon]\vec{E}(\omega) + [\sigma]\vec{E}(\omega) \tag{3.34}$$

To avoid computational errors caused by the high order of magnitude difference between electric and magnetic fields, Taflove [15] introduced a normalization of the magnetic field:

$$\tilde{H} = \sqrt{\frac{\mu_0}{\varepsilon_0}} H \tag{3.35}$$

Our new Maxwell's equations with normalized magnetic fields and PML tensor incorporated in becomes:

$$\nabla \times \vec{E}(\omega) = -j\omega \frac{[\mu_r]}{c_0}[S]\tilde{\vec{H}}(\omega) \tag{3.36}$$

$$\nabla \times \tilde{\vec{H}}(\omega) = j\omega \frac{[\varepsilon_r]}{c_0}[S]\vec{E}(\omega) + [\sigma]\eta_0\vec{E}(\omega) \tag{3.37}$$

Then the two-dimensional TM mode vector expansions of Eq. (3.36-3.37) are:

$$\frac{\partial E_z(\omega)}{\partial y} - \frac{\partial E_y(\omega)}{\partial z} = -j\omega \frac{\mu_{xx}}{c_0} s_x^{-1} s_y H_x(\omega) \tag{3.38}$$

$$\frac{\partial E_x(\omega)}{\partial z}-\frac{\partial E_z(\omega)}{\partial x}=-j\omega\frac{\mu_{yy}}{c_0}s_x s_y^{-1}H_y(\omega) \tag{3.39}$$

$$\frac{\partial H_y(\omega)}{\partial x}-\frac{\partial H_x(\omega)}{\partial y}=j\omega\frac{\varepsilon_{zz}}{c_0}s_x s_y E_z(\omega)+\sigma_{zz}\eta_0 E_z(\omega) \tag{3.40}$$

After replacing $s_{x,y,z}$ with $1+\sigma_{x,y,z}/j\omega\varepsilon_0$ and denotes CE_x, CE_y as the curl of $\vec{E}$ in x, y direction and CH_z as the curl of $\vec{H}$ in z direction, these equations become:

$$CE_x(\omega)=-j\omega\frac{\mu_{xx}}{c_0}\left(1+\frac{\sigma_x}{j\omega\varepsilon_0}\right)^{-1}\left(1+\frac{\sigma_y}{j\omega\varepsilon_0}\right)H_x(\omega) \tag{3.41}$$

$$CE_y(\omega)=-j\omega\frac{\mu_{yy}}{c_0}\left(1+\frac{\sigma_x}{j\omega\varepsilon_0}\right)\left(1+\frac{\sigma_y}{j\omega\varepsilon_0}\right)^{-1}H_y(\omega) \tag{3.42}$$

$$CH_z(\omega)=\eta_0\sigma_{zz}E_z(\omega)+j\omega\frac{\varepsilon_{zz}}{c_0}\left(1+\frac{\sigma_x}{j\omega\varepsilon_0}\right)\left(1+\frac{\sigma_y}{j\omega\varepsilon_0}\right)E_z(\omega) \tag{3.43}$$

They can then be reformed into:

$$j\omega H_x(\omega)+\frac{\sigma_y}{\varepsilon_0}H_x(\omega)=-\frac{c_0}{\mu_{xx}}CE_x(\omega)-\frac{\sigma_x c_0}{j\omega\varepsilon_0\mu_{xx}}CE_x(\omega) \tag{3.44}$$

$$j\omega H_y(\omega)+\frac{\sigma_x}{\varepsilon_0}H_y(\omega)=-\frac{c_0}{\mu_{yy}}CE_y(\omega)-\frac{c_0\sigma_y}{j\omega\varepsilon_0\mu_r}CE_y(\omega) \tag{3.45}$$

$$j\omega\varepsilon_{zz}E_z(\omega)+\frac{\sigma_x+\sigma_y}{\varepsilon_0}E_z(\omega)+\frac{\sigma_x\sigma_y}{j\omega\varepsilon_0^2}E_z(\omega)+\frac{\sigma_{zz}}{\varepsilon_0}E_z(\omega)=c_0CH_z(\omega) \tag{3.46}$$

These equations can be transformed from frequency domain into time domain functions with a reverse Fourier transform as:

$$\frac{\partial H_x(t)}{\partial t}+\frac{\sigma_y}{\varepsilon_0}H_x(t)=-\frac{c_0}{\mu_{xx}}CE_x(t)-\frac{c_0\sigma_x}{\varepsilon_0\mu_{xx}}\int_{-\infty}^{t}CE_x(t)\,dt \tag{3.47}$$

$$\frac{\partial H_y(t)}{\partial t}+\frac{\sigma_x}{\varepsilon_0}H_y(t)=-\frac{c_0}{\mu_{yy}}CE_y(t)-\frac{c_0\sigma_y}{\varepsilon_0\mu_{yy}}\int_{-\infty}^{t}CE_y(t)\,dt \tag{3.48}$$

$$\frac{\varepsilon_{zz}(t)\partial E_z(t)}{\partial t}+\left(\frac{\sigma_x+\sigma_y}{\varepsilon_0}\right)E_z(t)+\frac{\sigma_{zz}(t)}{\varepsilon_0}E_z(t)+\frac{\sigma_x\sigma_y}{\varepsilon_0^2}\int_{-\infty}^{t}E_z(t)\,dt=c_0CH_z(t) \tag{3.49}$$

Note that $\varepsilon_{zz}(t)$ and $\sigma_{zz}(t)$ in Eq. (3.49) are functions of time because our simulations involve oscillating devices that have time-varying properties, the details will be illustrated in Section 4.3.

Recall that in the Yee grid, there is a half temporal difference between the electric and magnetic fields. For instance, $\vec{E}$ components at time t have their corresponding $\vec{H}$ components sampled at time $t-\Delta t/2$ and $t+\Delta t/2$, thus $\vec{H}$ components at time t should be estimated by averaging the values of $t-\Delta t/2$ and $t+\Delta t/2$. Let's specify that in Eq. (3.47-3.49), the curl of $\vec{E}$ exists at time t and the curl of $\vec{H}$ exists at $t+\Delta t/2$, that were previously calculated through spatial approximations in Eq. (3.18-3.20). Then apply temporal central-difference approximations for derivatives in Eq. (3.47-3.49) and estimate integrals with summations yields:

$$\frac{H_x\left(t+\frac{\Delta t}{2}\right)-H_x\left(t-\frac{\Delta t}{2}\right)}{\Delta t}+\frac{\sigma_y}{\varepsilon_0}\frac{H_x\left(t+\frac{\Delta t}{2}\right)+H_x\left(t-\frac{\Delta t}{2}\right)}{2}=-\frac{c_0}{\mu_{xx}}CE_x(t)-\frac{c_0\sigma_x\Delta t}{\varepsilon_0\mu_{xx}}\sum_{T=0}^{t}CE_x(T) \tag{3.50}$$

$$\frac{H_y\left(t+\frac{\Delta t}{2}\right)-H_y\left(t-\frac{\Delta t}{2}\right)}{\Delta t}+\frac{\sigma_x}{\varepsilon_0}\frac{H_y\left(t+\frac{\Delta t}{2}\right)+H_y\left(t-\frac{\Delta t}{2}\right)}{2}=-\frac{c_0}{\mu_{yy}}CE_y(t)-\frac{c_0\sigma_y\Delta t}{\varepsilon_0\mu_{yy}}\sum_{T=0}^{t}CE_y(T) \tag{3.51}$$

$$\frac{\varepsilon_{zz}(t+\Delta t)+\varepsilon_{zz}(t)}{2}\cdot\frac{E_z(t+\Delta t)-E_z(t)}{\Delta t}+\frac{\sigma_x+\sigma_y}{\varepsilon_0}\cdot\frac{E_z(t+\Delta t)+E_z(t)}{2}+\frac{\sigma_{zz}(t+\Delta t)+\sigma_{zz}(t)}{2\varepsilon_0}E_z(t)$$

$$+\frac{\sigma_x\sigma_y\Delta t}{\varepsilon_0^2}\left[\frac{E_z\left(t+\Delta t\right)+E_z\left(t\right)}{4}+\sum_{T=0}^{t}E_z\left(T\right)\right]=c_0CH_z\left(t+\frac{\Delta t}{2}\right) \tag{3.52}$$

By examining the above equations, it is evident that future field components $H_x(t+\Delta t/2)$, $H_y(t+\Delta t/2)$ and $E_z(t+\Delta t)$ can be calculated with current field components and known variables, thus the update equation for them can be derived as:

$$H_x\left(t+\frac{\Delta t}{2}\right)=\frac{\left(\frac{1}{\Delta t}-\frac{\sigma_y}{2\varepsilon_0}\right)H_x\left(t-\frac{\Delta t}{2}\right)-\frac{c_0}{\mu_{xx}}CE_x\left(t\right)-\frac{c_0\sigma_x\Delta t}{\varepsilon_0\mu_{xx}}\sum_{T=0}^{t}CE_x\left(t\right)}{\left(\frac{1}{\Delta t}+\frac{\sigma_y}{2\varepsilon_0}\right)} \tag{3.53}$$

$$H_y\left(t+\frac{\Delta t}{2}\right)=\frac{\left(\frac{1}{\Delta t}-\frac{\sigma_x}{2\varepsilon_0}\right)H_y\left(t-\frac{\Delta t}{2}\right)-\frac{c_0}{\mu_{yy}}CE_y\left(t\right)-\frac{c_0\sigma_y\Delta t}{\varepsilon_0\mu_{yy}}\sum_{T=0}^{t}CE_y\left(t\right)}{\left(\frac{1}{\Delta t}+\frac{\sigma_x}{2\varepsilon_0}\right)} \tag{3.54}$$

$$E_z\left(t+\Delta t\right)=\frac{\left[\frac{\varepsilon_{zz}\left(t+\Delta t\right)+\varepsilon_{zz}\left(t\right)}{2\Delta t}-\frac{\sigma_x+\sigma_y}{2\varepsilon_0}-\frac{\sigma_{zz}\left(t+\Delta t\right)+\sigma_{zz}\left(t\right)}{2\varepsilon_0}-\frac{\sigma_x\sigma_y\Delta t}{4\varepsilon_0^2}\right]E_z\left(t\right)+\ldots}{\frac{\varepsilon_{zz}\left(t+\Delta t\right)+\varepsilon_{zz}\left(t\right)}{2\Delta t}+\frac{\sigma_x+\sigma_y}{2\varepsilon_0}+\frac{\sigma_{zz}\left(t+\Delta t\right)+\sigma_{zz}\left(t\right)}{2\varepsilon_0}+\frac{\sigma_x\sigma_y\Delta t}{4\varepsilon_0^2}}$$

$$\frac{c_0CH_z\left(t\right)-\frac{\sigma_x\sigma_y\Delta t}{\varepsilon_0^2}\sum_{T=0}^{t}E_z\left(T\right)}{} \tag{3.55}$$

To further simplify our FDTD algorithm formulation, the non-time varying terms are collected as coefficients:

$$mHx0=\left(\frac{1}{\Delta t}+\frac{\sigma_y}{2\varepsilon_0}\right) \qquad mHx1=\left(\frac{1}{\Delta t}-\frac{\sigma_y}{2\varepsilon_0}\right)/\,mHx0$$

$$mHx2 = \frac{c_0}{\mu_{xx}} / mHx0 \qquad mHx3 = \frac{c_0 \sigma_x \Delta t}{\varepsilon_0 \mu_{xx}} / mHx0$$

$$mHy0 = \left(\frac{1}{\Delta t} + \frac{\sigma_x}{2\varepsilon_0} \right) \qquad mHy1 = \left(\frac{1}{\Delta t} - \frac{\sigma_x}{2\varepsilon_0} \right) / mHy0$$

$$mHy2 = \frac{c_0}{\mu_{yy}} / mHy0 \qquad mHy3 = \frac{c_0 \sigma_y \Delta t}{\varepsilon_0 \mu_{yy}} / mHy0$$

$$mEz1 = \frac{\sigma_x + \sigma_y}{2\varepsilon_0} + \frac{\sigma_x \sigma_y \Delta t}{4\varepsilon_0^2} \qquad mEz2 = \frac{\sigma_x \sigma_y \Delta t}{\varepsilon_0^2}$$

Since they are primarily comprised of constants and parameters that do not change once set, it would be much more computationally efficient to precompute them beforehand, store them as a lookup table that can be easily accessible during the simulation. The new update equation becomes:

$$H_x\left(t + \frac{\Delta t}{2}\right) = mHx1 H_x\left(t - \frac{\Delta t}{2}\right) - mHx2 CE_x(t) - mHx3 \sum_{T=0}^{t} CE_x(T) \tag{3.56}$$

$$H_y\left(t + \frac{\Delta t}{2}\right) = mHy1 H_y\left(t - \frac{\Delta t}{2}\right) - mHy2 CE_y(t) - mHy3 \sum_{T=0}^{t} CE_y(T) \tag{3.57}$$

$$E_z(t + \Delta t) = \frac{\left(\frac{\varepsilon_{zz}(t + \Delta t) + \varepsilon_{zz}(t)}{2\Delta t} - \frac{\sigma_{zz}(t + \Delta t) + \sigma_{zz}(t)}{2\varepsilon_0} - mEz1 \right) E_z(t) + \ldots}{\frac{\varepsilon_{zz}(t + \Delta t) + \varepsilon_{zz}(t)}{2\Delta t} + \frac{\sigma_{zz}(t + \Delta t) + \sigma_{zz}(t)}{2\varepsilon_0} + mEz1}$$

$$\frac{c_0 CH_z\left(t + \frac{\Delta t}{2}\right) - mEz2 \sum_{T=0}^{t} E_z(T)}{} \tag{3.58}$$

With update equations for all components in Faraday's law and Ampere's law, an FDTD simulation process can be illustrated in Figure.3 which forms the foundation of our simulations.

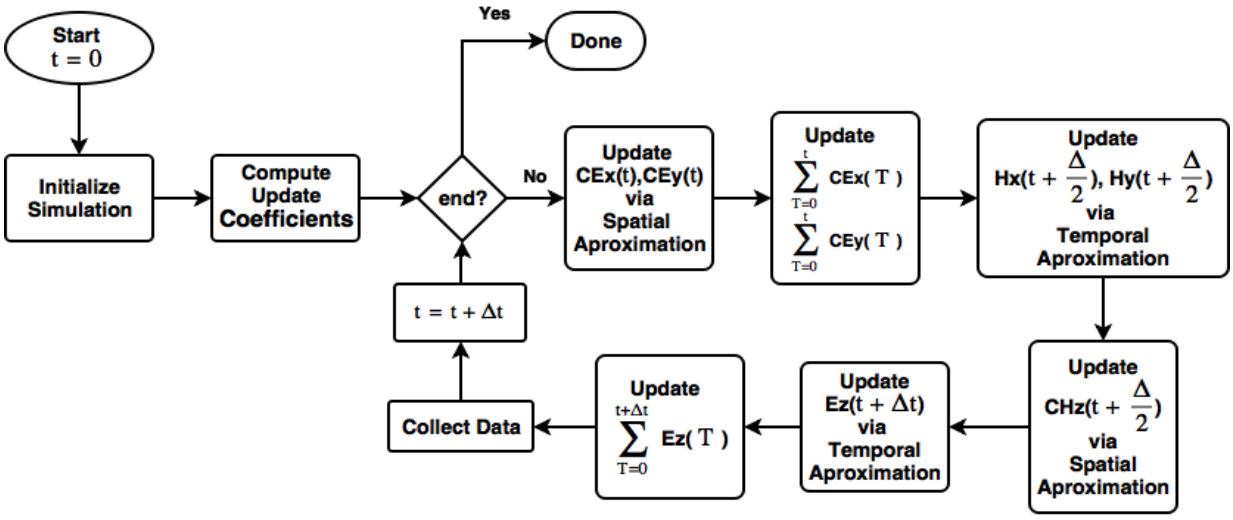

Figure 3. Flowchart of FDTD simulation in a 2-D TM mode

3.7 Other Conditions for FDTD Simulations

For our spatial and temporal estimations, it's important that a sufficiently small δ for central-difference approximations was chosen, it has been verified that at least ten cells per wavelength are necessary to ensure an acceptable accuracy for spatial approximations, although a higher resolution may be needed for more complex devices. Once a spatial size has been chosen, the temporal difference needs to be determined by the Courant-Friedrichs-Lewy stability condition [20]:

$$\Delta t \leq \left(c_0 \sqrt{\frac{1}{\Delta x^2} + \frac{1}{\Delta y^2} + \frac{1}{\Delta z^2}} \right)^{-1} \tag{3.59}$$

A common choice for Δt to ensure stability and accuracy on any grid design is given as:

$$\Delta t = \frac{\min(\Delta x, \Delta y, \Delta z)}{2c_0} \tag{3.60}$$

This expression also has the benefit that fields will travel exactly one grid cell in two time-steps in free space.

3.8 Source Excitations

There are different types of source signals suited for different purposes, two are used in this project, Gaussian pulse and sinusoidal continuous excitation. A Gaussian function can be expressed as:

$$g(t) = e^{-\frac{(t-t_0)^2}{t_\omega^2}} \tag{3.61}$$

Where t_0 is the temporal delay and t_ω is the half-width of the Gaussian function. Typically, t_0 is chosen to be greater than $4t_\omega$ to avoid the simulation start inside the pulse. As for the choice of t_ω, the Gaussian pulse has the characteristic of simulating a board range of frequencies tops at $1/\pi t_\omega \leq f_{max} \leq 2/\pi t_\omega$, thus for a maximum frequency, a half-width could be chosen as $t_\omega = 0.5/f_{max}$ in this range.

A sinusoidal source as a function of time can be written as $\sin(2\pi f t)$, however, it cannot be turned on instantaneously, rather be turned on with a smoothing function at the beginning, in our case a half Gaussian pulse. This can be achieved by creating a regular Gaussian pulse same as Eq. (3.61) and replace the value for $t > t_0$ with ones:

$$s(t) = \begin{cases} g(t)\sin(2\pi f t) & for \quad 0 < t \leq t_0 \\ 1 \times \sin(2\pi f t) & \quad\quad t > t_0 \end{cases} \tag{3.62}$$

Where t_0 should not only be the peak of the Gaussian but also one of the peaks the sine function. This can be accomplished by choosing a small integer number n and set $t_0 = (4n+1)/4f$.

3.9 Total-field/Scattered-field Formulation

For problems that employ a plane wave excitation, directly modelling the source would be a substantial computational burden since it must exist far beyond the problem domain for

the wave fronts being parallel when they reach the devices. Thus, a method for injecting already paralleled waves directly into the problem domain is required. The most opportune one was proposed in [21], now commonly referred to as the total-field/scattered-field (TF/SF) formulation, assumes that the actual physical total electric and magnetic fields $\vec{E}_{total}$ and $\vec{H}_{total}$ can be split into:

$$\vec{E}_{total} = \vec{E}_{inc} + \vec{E}_{scat} \tag{3.63}$$

$$\vec{H}_{total} = \vec{H}_{inc} + \vec{H}_{scat} \tag{3.64}$$

Where the incident-fields $\vec{E}_{inc}$ and $\vec{H}_{inc}$ are fields propagating through the problem domain without any interaction with simulated devices. The scattered-fields $\vec{E}_{scat}$ and $\vec{H}_{scat}$ are fields initially unknown and only affected by wave scattered by simulated devices. In reality, the boundary between the total-field and scattered field serves as an absorbing boundary condition that only absorbs excitation waves.

Figure.4 illustrates the total-field and scattered-field in the Yee grid. Consider the positions that have $j = j_0$ where the scattered-field components E_z and H_y are located. Recall that the curl of E on x direction exists at the same spatial location as H_x which reside in the total-field, to compute the CE_x^{i,j_0} with our spatial approximations in Eq. (3.18), we need the corresponding E_z at (i, j_0) and $(i, j_0 + 1)$. However, $E_{z,total}^{i,j_0}$ does not exist because (i, j_0) is located inside the scattered-field, therefore, CE_x^{i,j_0} cannot be directly calculated.

Yet, since

$$E_{x,total}^{i,j_0} = E_{x,scat}^{i,j_0} + E_{x,inc}^{i,j_0} \tag{3.65}$$

CE_x^{i,j_0} can still be calculated with:

$$CE_x^{i,j_0} = \frac{E_{z,total}^{i,j_0+1} - E_{z,total}^{i,j_0}}{\Delta y} = \frac{E_{z,total}^{i,j_0+1} - \left(E_{z,scat}^{i,j_0} + E_{z,inc}^{i,j_0}\right)}{\Delta y} = \frac{E_{z,total}^{i,j_0+1} - E_{z,scat}^{i,j_0}}{\Delta y} - \frac{E_{z,inc}^{i,j_0}}{\Delta y} \quad (3.66)$$

Note that the first two terms are equivalent to Eq. (3.18), which means CE_x^{i,j_0} can be computed normally without considering the TF/SF condition then subtract the incident terms at $j = j_0$:

$$CE_x^{i,j_0} = CE_x^{i,j_0}\Big|^{Eq.(3.18)} - \frac{E_{z,inc}^{i,j_0}}{\Delta y} \quad (3.67)$$

Similarly, CH_z^{i,j_0} located in the scattered-field can be calculated with H_x located at $(i, j_0 + 1/2)$ inside the total-field and Eq. (3.20) as:

$$CH_z^{i,j_0} = \frac{H_{y,scat}^{i+1/2,j} - H_{y,scat}^{i-1/2,j}}{\Delta x} - \frac{\left(H_{x,total}^{i,j_0+1/2} - H_{x,scat}^{i,j_0-1/2}\right) - H_{x,inc}^{i,j_0+1/2}}{\Delta y}$$

$$= CH_z^{i,j_0}\Big|^{Eq.(3.20)} + \frac{H_{x,inc}^{i,j_0+1/2}}{\Delta y} \quad (3.68)$$

Now consider the situation on the opposite side where $j = j_1$. To compute CE_x^{i,j_1-1} and CH_z^{i,j_1} requires E_z in the scattered-field (i, j_1) and H_x in the total-field $(i, j_1 - 1/2)$. Similar to $j = j_0$, CE_x^{i,j_1-1} and CH_z^{i,j_1} can be computed normally then add or subtract the incident term at the boundary as:

$$CE_x^{i,j_1-1} = CE_x^{i,j_1-1}\Big|^{Eq.(3.18)} + \frac{E_{z,inc}^{i,j_1}}{\Delta y} \quad (3.69)$$

$$CH_z^{i,j_1} = CH_z^{i,j_1}\Big|^{Eq.(3.20)} - \frac{H_{x,inc}^{i,j_1+1/2}}{\Delta y} \quad (3.70)$$

For $i = i_0$, $E_z^{i_0,j}$ in the scattered-field is required to calculate $CE_y^{i_0,j}$, and $CH_z^{i_0,j}$ can be computed with $H_y^{i_0+1/2,j}$ in the total-field as:

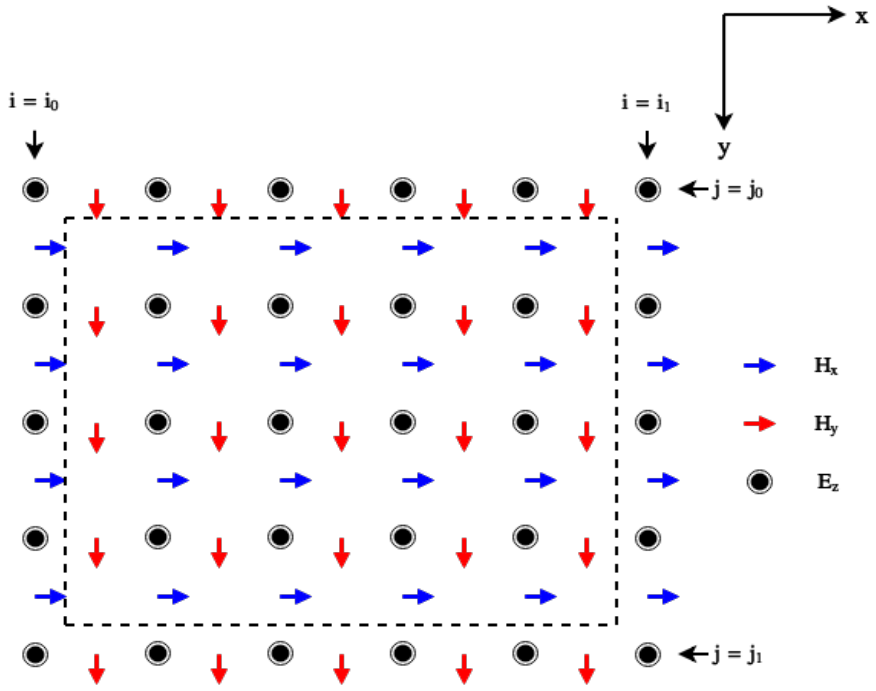

Figure 4. Field components in the 2-D TM mode grid at the boundaries of the total-field and scattered-field regions for plane wave exaction. Note the total-field is the region bounded by dashed lines. And regions outside are scattered-field.

$$CE_y^{i_0,j} = \frac{E_{z,total}^{i_0+1,j} - E_{z,scat}^{i_0,j}}{\Delta x} + \frac{E_{z,inc}^{i_0,j}}{\Delta x} \tag{3.71}$$

$$CH_z^{i_0,j} = \frac{H_{y,total}^{i_0+1/2,j} - H_{y,scat}^{i_0-1/2,j}}{\Delta x} - \frac{H_{x,scat}^{i_0,j+1/2} - H_{x,scat}^{i_0,j-1/}}{\Delta y} - \frac{H_{y,inc}^{i_0+1/2,j}}{\Delta x} \tag{3.72}$$

They also can be calculated by computing our $CE_y^{i_0,j}$ and $CH_z^{i_0,j}$ normally with Eq. (3.19-3.20) without considering TF/SF condition then correct with incident terms at $i = i_0$.

$$CE_y^{i_0,j} = CE_y^{i_0,j}\,|^{Eq.(3.19)} + \frac{E_{z,inc}^{i_0,j}}{\Delta x} \tag{3.73}$$

$$CH_z^{i_0,j} = CH_z^{i_0,j}\,|^{Eq.(3.20)} - \frac{H_{y,inc}^{i_0+1/2,j}}{\Delta x} \tag{3.74}$$

At $i = i_1$, $E_z^{i_1,j}$ in the scattered-field is required to compute $CE_y^{i_1-1,j}$, $CH_z^{i_1,j}$ can be computed with $H_y^{i_1-1/2,j}$ in the total-field:

$$CE_y^{i_1,j} = CE_y^{i_0,j} \Big|^{Eq.(3.19)} - \frac{E_{z,inc}^{i_1+1,j}}{\Delta x} \tag{3.75}$$

$$CH_z^{i_1,j} = CH_z^{i_1,j} \Big|^{Eq.(3.20)} + \frac{H_{y,inc}^{i_1-1/2,j}}{\Delta x} \tag{3.76}$$

Together, these corrections properly separate the total-field and scattered-field for our two-dimensional TM mode grid, note that different placements of the TF/SF boundary will result in slightly different formulations. After implementing these corrections, a numerical plane wave can be generated in the total-field region propagating through the total-field region and being perfectly absorbed once hit the TF/SF boundary. By positioning the incident plane right next to a boundary, fields propagate toward that boundary will be absorbed immediately, thus appear as a plane wave propagating in the opposite direction. In addition, the boundaries between total-field and scattered-field are transparent to all outgoing scattered waves, permitting them to pass without reflection or refraction.

3.10 Correction Terms for TF/SF

The crucial part of the TF/SF formulation is the correction terms. As previously defined, the incident-field is the source signal propagating through problem domain without interacting with simulated devices. One way of doing this is to simulate an identical secondary grid alongside our main grid with nothing except PML. In this project, the plane wave source is defined as propagating along y axis. For the interface where $j = j_0$, since a plane wave only changes in the direction of its propagation, and this interface is norm to y axis, all the incident terms on this interface will have the same value, the same also goes to the interface where $j = j_1$. As for interface where $i = i_0$ and $i = i_1$, because the incident wave does not interact with anything, their value should be changing identically, only one of them need to be computed. Since the incident wave propagates in y direction, there are

no x component contributes to our $\vec{H}$ field, therefore, our secondary grid can be reduced to a one-dimensional grid that can reuse our existing formulations.

4. FDTD with an Oscillating Object

In this section, a brief introduction of Raman scattering effect is outlined. And then a detailed description of the methodology used to incorporate an oscillating cylinder in our FDTD algorithm will be given.

4.1 Raman Effect

When light incident on a small system, most of it will be scattered without any change in frequency. This is called Rayleigh Scattering after physicist Lord Rayleigh. A fraction of the scattering is inelastic and referred to as Raman scattering. Such scattering with a change in frequency was discovered by C.V. Raman in 1928 [22]. A detailed description of the effect could be found in [23], but to summarize:

When Light is incident onto a system, it induces a dipole moment p, which can be described as:

$$p = a \cdot \vec{E} \tag{4.1}$$

Where a is the polarizability of the system, $\vec{E}$ is the electric field of the incident signal traveling at frequency f with an amplitude of $\vec{E}_0$, for a sinusoidal signal it can be given by:

$$\vec{E} = \vec{E}_0 \sin\left(2\pi f t\right) \tag{4.2}$$

A vibrating system with frequency f_v will change the polarizability of itself, resulting in the polarizability oscillating at f_v:

$$a = a_0 + \beta \sin\left(2\pi f_v t\right) \tag{4.3}$$

Where a_0 is the polarizability in equilibrium configuration, and β is the variation of polarizability associated with system's vibration. Combine Eq. (4.1-4.3), the induced dipole becomes:

$$p = a_0 E_0 sin(2\pi ft) + \beta E_0 \sin(2\pi ft)\sin(2\pi f_v t) \tag{4.4}$$

Appling the trigonometric relations $\sin(A)\sin(B) = [\cos(A-B) - cos(A+B)]/2$ it becomes:

$$p = a_0 \vec{E}_0 sin(2\pi ft) + \frac{1}{2}\beta \vec{E}_0 \left\{\cos\left[2\pi(f - f_v)t\right] - \cos\left[2\pi(f + f_v)t\right]\right\} \tag{4.5}$$

This indicates the oscillating dipole will not only radiate light at frequency f but also radiate light weakly at $f + f_v$and $f - f_v$ which give rise to Raman scattering. $f - f_v$ is called the Stokes frequency shift, $f + f_v$ is referred to as the Anti-Stokes frequency shift. To mimic this effect, an oscillating cylinder will be modeled for our FDTD simulation in the next section.

4.2 Implementing Oscillating Device

In FDTD simulations, devices within the problem domain are defined by specifying permittivity, permeability and conductivity values of each grid that represent the devices. For most materials, permeability is set to free-space since the material is not magnetizable, thus permeability will not be discussed further outside the FDTD formulations. To realize changes of a device's profile, only need to change the permittivity and conductivity values of the grid. An oscillating cylindrical rod in a two-dimensional grid can be represented with a circle that oscillates into ellipses. Consider an ellipse equation in a two-dimensional coordinate system, the area within it could be expressed as:

$$\frac{(x-x_0)^2}{a^2} + \frac{(y-y_0)^2}{b^2} \le 1 \qquad \text{or} \qquad \frac{(x-x_0)^2}{b^2} + \frac{(y-y_0)^2}{a^2} \le 1 \tag{4.6}$$

Where (x_0, y_0) is the center of the ellipse, a and b are its major and minor axes for which we define $a \ge b$. And once $a = b$ is satisfied, this function will also represent a circle. By oscillating the value of a and b periodically, the device can be modeled with periodic

oscillation. Given an oscillation frequency f_v , the period would be $p = {f_v}^{-1}$, then this period needs to be divided into four fractions.

For the first quarter, that is, any time t that satisfies the condition of $0 \le t \bmod p \le p/4$, our device should gradually transform from a circle with radius $r = \frac{a+b}{2}$ to an ellipse as a function of time:

$$O(t) = \frac{(x - x_0)^2}{(r + \Delta dt')^2} + \frac{(y - y_0)^2}{(r - \Delta dt')^2} \le 1 \tag{4.7}$$

Where $t' = t \bmod \frac{p}{4}$ is a periodic time-step, Δd is a small variation in length that equals to $4d_{max}/p$, and d_{max} is a maximum deformation, thus have the relations:

$$\begin{cases} r + \Delta dt' = a \\ r - \Delta dt' = b \end{cases} \quad \text{for} \quad t \bmod p = \frac{p}{4}, \frac{p}{2}, \frac{3p}{4}, p \tag{4.8}$$

For the second quarter that has $p/4 \le t \bmod p \le p/2$, our device should transform from the ellipse back to its equilibrium form with a function:

$$O(t) = \frac{(x - x_0)^2}{(a - \Delta dt')^2} + \frac{(y - y_0)^2}{(b + \Delta dt')^2} \le 1 \tag{4.9}$$

In the third quarter that has $p/2 \le t \bmod p \le 3p/4$, the device deforms into ellipse same as in the first section but in the opposite direction:

$$O(t) = \frac{(x - x_0)^2}{(r - \Delta dt')^2} + \frac{(y - y_0)^2}{(r + \Delta dt')^2} \le 1 \tag{4.10}$$

And at last, the device returns to its equilibrium in the fourth quarter period:

$$O(t) = \frac{(x - x_0)^2}{(b + \Delta dt')^2} + \frac{(y - y_0)^2}{(a - \Delta dt')^2} \le 1 \tag{4.11}$$

These formulations could be implemented numerically by creating two matrixes X, Y representing the coordinate system, each row of X is a full copy of all x coordinates, i.e. $X(i,:) = i$ for i =1, 2, 3… and each column of Y contains the copy of all y coordinates $Y(:,j) = j$. Then by applying these formulations, the logic operator <= which correspond to less than equal will return a logical matrix with coordinates (i, j) outside the devices marked as false and those within the device mark as true. Since true and false are stored as one and zero in computer memory, the coordination information contained in this matrix can be straightforwardly turned into permittivity and conductivity matrixes as:

$$\varepsilon_r(t) = (\varepsilon_{r1} - \varepsilon_{r2})O(t) + \varepsilon_{r2} \qquad \sigma(t) = (\sigma_{r1} - \sigma_{r2})O(t) + \sigma_{r2} \tag{4.12}$$

Where O is the logical matrix previously mentioned, and every note in the grid that represents our device has a relative permittivity of ε_{r1} and conductivity of σ_{r1} , yet other positions have relative permittivity ε_{r2} and conductivity σ_{r2} which were set to one and zero to represent frees pace in this project.

4.3 Update Equation with Time-varying Property

By oscillating our device, these properties become time-varying instead of constant compared to Yee's formulation and most common FDTD algorithms. An independently time-varying permittivity and conductivity can be written as:

$$[\varepsilon] = \varepsilon_0 \varepsilon_r(t) \qquad [\sigma] = \sigma(t) \tag{4.13}$$

Replace the terms in Eq. (3.9) result in:

$$\nabla \times \vec{H} = \varepsilon_0 \varepsilon_r(t) \frac{\partial \vec{E}}{\partial t} + \sigma(t)\vec{E} \tag{4.14}$$

Recall that the curl of magnetic field exists at the same temporal position as magnetic field that has a half temporal difference with electric field, hence for the curl of $\vec{H}$ at given time t its corresponding $\vec{E}$ field and electric properties should exist at $t + \Delta/2$, therefore:

$$CH\left(t\right) = \varepsilon_0 \varepsilon_r \left(t + \frac{\Delta t}{2}\right) \frac{\partial \vec{E}\left(t + \frac{\Delta t}{2}\right)}{\partial t} + \sigma\left(t + \frac{\Delta t}{2}\right) \vec{E}\left(t + \frac{\Delta t}{2}\right) \tag{4.15}$$

Same as the electric field, the permittivity and conductivity at time $t + \Delta/2$ also can be estimated by averaging the values at t and $t + \Delta t$. Thus, after applying temporal approximation for our electric field on z direction, the formulation becomes:

$$CHz\left(t\right) = \varepsilon_0 \frac{\varepsilon_{zz}\left(t + \Delta t\right) + \varepsilon_{zz}\left(t\right)}{2} \frac{E_z\left(t + \Delta t\right) - E_z\left(t\right)}{\Delta t} + \frac{\sigma\left(t + \Delta t\right) + \sigma\left(t\right)}{2} \frac{E_z\left(t + \Delta t\right) + E_z\left(t\right)}{2} \tag{4.16}$$

Which will result in our Eq. (3.52) formulation once perfectly matched layer is incorporated.

However, there will be a drawback in achieving oscillation by changing the grid properties. Abrupt alteration in the state of the medium will affect the characteristics of fields exist within this medium. Specifically, this happens on the boundary of our device that changes its relative permittivity when it expands or contracts.

4.4 Transitional-layer

To address the boundary problem, an additional transition-layer was implemented on the boundary of our device, aiming at drastically smoothening the variation of permittivity, so the change of permittivity becomes slow enough to be considered as time-invariant. Recall the formulation of our oscillation in Eq. (4.7-4.11), since these formulations exist on a grid system, all the variables should be integers except Δd which equals to $4d_{max}/p$, the ellipse

would only change once per Δd^{-1} time-steps when $\Delta d \cdot t'$ reaches an integer. By anticipating how the ellipse would change next time, the Δd^{-1} time-steps can be utilized to integrate linearly increasing or decreasing functions to make permittivity alterations much smoother during the simulation. Consider our formulation of the first periodical section Eq. (4.7), after Δd^{-1} time-steps the function becomes:

$$O\left(t+\ \Delta d^{-1}\right)=\frac{\left(x-x_0\right)^2}{\left(r+\Delta dt'+1\right)^2}+\frac{\left(y-y_0\right)^2}{\left(r-\Delta dt'-1\right)^2}\leq 1 \tag{4.17}$$

Where the oscillation is expanding in x direction and contracting in y direction, subtracting $O(t+\ \Delta d^{-1})$ by $O(t)$ yields a matrix with coordinate information of changes between two time-steps. As illustrated in Figure.5, points in area E would be zero indicate invariant, points in A and B would have a value of one indicate expansion, and points inside C and D have a value of negative one indicates contraction. Note that Figure.5 is not an accurate representation, A, B, C, D would be a thin layer of grids that have the thickness of one grid. The permittivity change in respect of time can be characterized as a function:

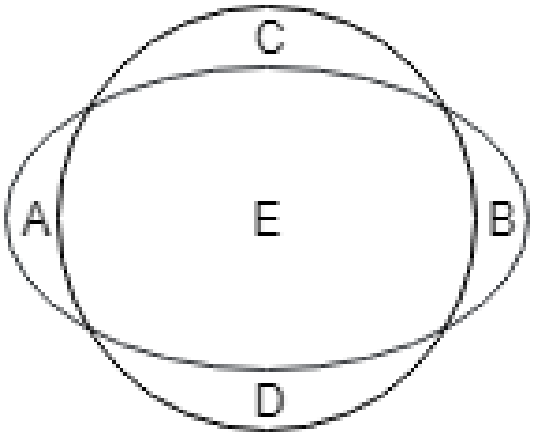

Figure 5. Representation of ellipse oscillating during first quarter of the period. A, B are expanding, C, D are contracting.

$$\varepsilon_{\Delta}(t) = \frac{t \bmod \Delta d^{-1}}{\Delta d^{-1}}(\varepsilon_{r2} - \varepsilon_{r1}) \tag{4.18}$$

Our permittivity function with transition-layer build-in then becomes:

$$\varepsilon_r(t) = (\varepsilon_{r1} - \varepsilon_{r2})O(t) + \varepsilon_{r2} + \varepsilon_{\Delta}(t)\left[O\left(t + \Delta d^{-1}\right) - O(t)\right] \tag{4.19}$$

With a relatively slow oscillation compared to the incident frequency and a reasonable oscillation amplitude, the relative permittivity variation can be effectively stretch to at least -3 orders of magnitude per time-step without noticeable stability issues.

5. Results

With the system described in previous sections, several simulations were designed to validate if the system is working as expected and giving us some insight on how the electromagnetic fields react to an oscillating device. The geometry of the simulation was set up as in Figure.6. An oscillating device is located in the middle of the grid and surrounded by the TF/SF boundaries, the device is inside the total-field and an observation point is located in the scattered field perpendicular to the y axis. A sinusoidal plane wave source was incident next to the boundary in the total-field, so the incident wave will only travel in y + direction. The oscillatory motion will start after the continuous wave filled the problem domain. Fields passing through the observation point will be recorded during the simulation, so the spectrum of the field can be obtained using Fourier transform after the system reaches a steady state. By changing the parameters of the system such as the incident frequency, diameter of the device, etc., how the fields interact with different configurations will be studied.

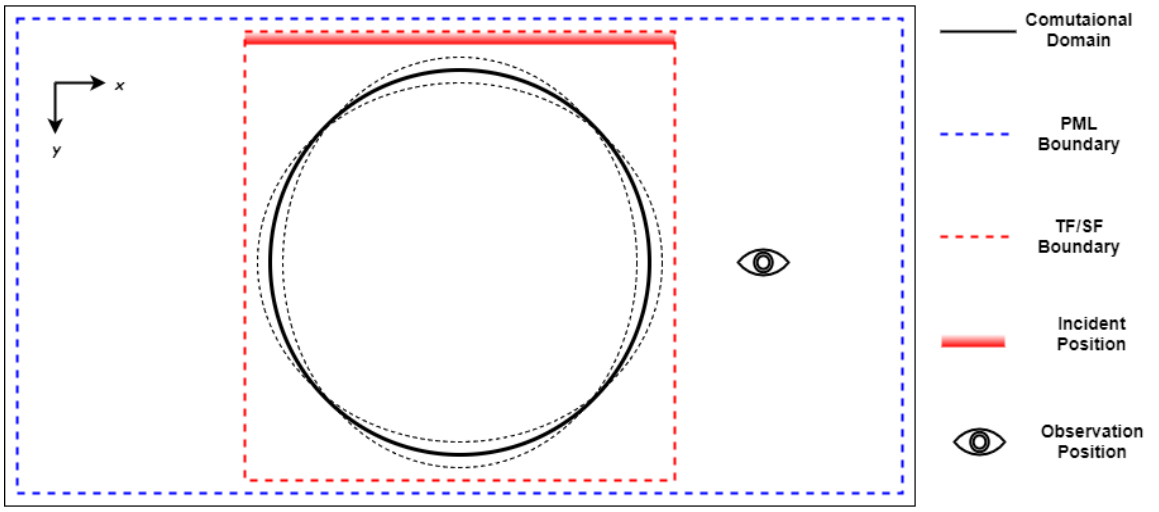

Figure 6. Schematic of the simulation setup, the computational domain is represented by the most outside solid line, area between the solid line and the blue dash line is 10 cells deep PML. Total-field/Scattered-field boundaries are surrounding the oscillating device in the middle. And the incident position next to the Total-field/Scattered field boundary.

5.1 Raman Sidebands

In these simulations, the goal is to test whether the Raman sidebands can be observed with our implementation, a device was simulated with the diameter of 3 micrometers and a refractive index of 1.9 to be representative of common materials. The oscillation amplitude i.e. the max deformation was set to be 10% of the radius and the mechanical frequency was set to 20 terahertz in order to balance between a smooth transition of the permittivity during oscillation and a reasonable simulation run time being required to bring the system to a steady state. Two different incident wavelengths were considered, the first one is 500nm chosen within the wavelength of visible light, the second frequency has a slightly larger wavelength than the diameter of our device. As shown in Figure.7-8, noticeable sidebands

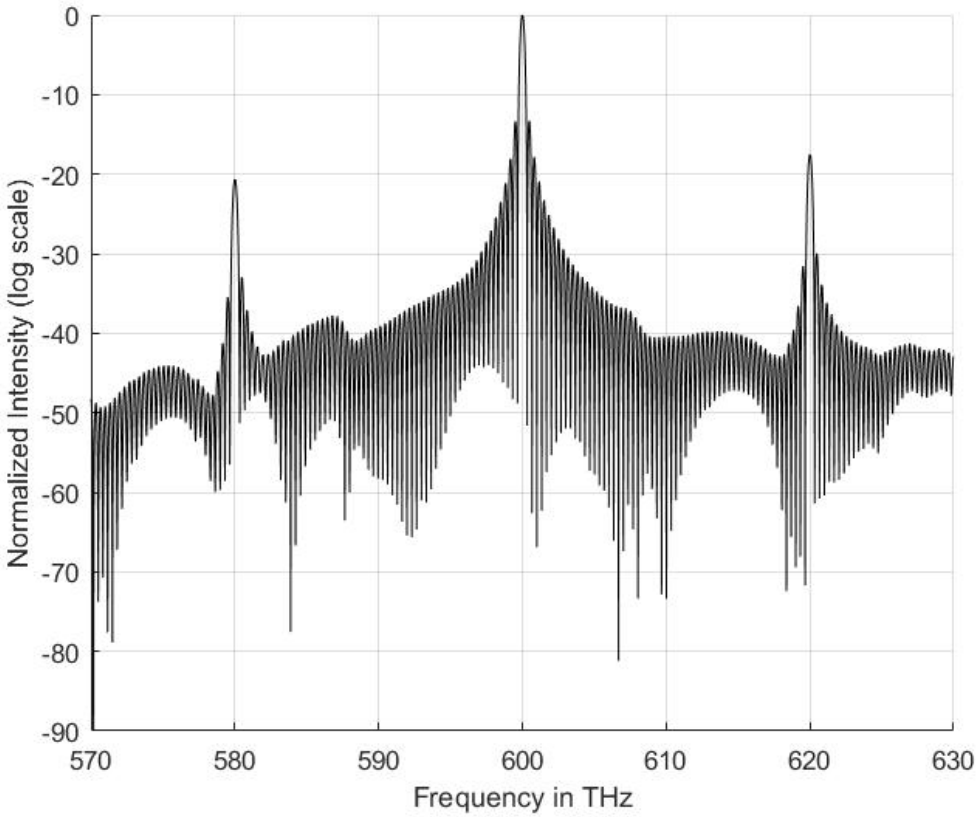

Figure 7. Spectrum of the Raman scattering observed with the incident frequency of 600Thz, and oscillation frequency set as 20THz, Stokes shift appeared at 580Thz and anti-Stokes at 620 THz.

can be observed with both incident wavelengths that are in line with our expedition of the Raman effect. Figure.7-8 shows that in both cases anti-Stokes shifts are noticeably stronger than and Stokes shift, which is also to be anticipated by Raman scattering. But we did not expect the difference between the intensity was amplified by increasing the wavelength. However, this may not be the characteristic of Raman scattering, but the enhancement of Raman scattering caused by whisper gallery mode resonance.

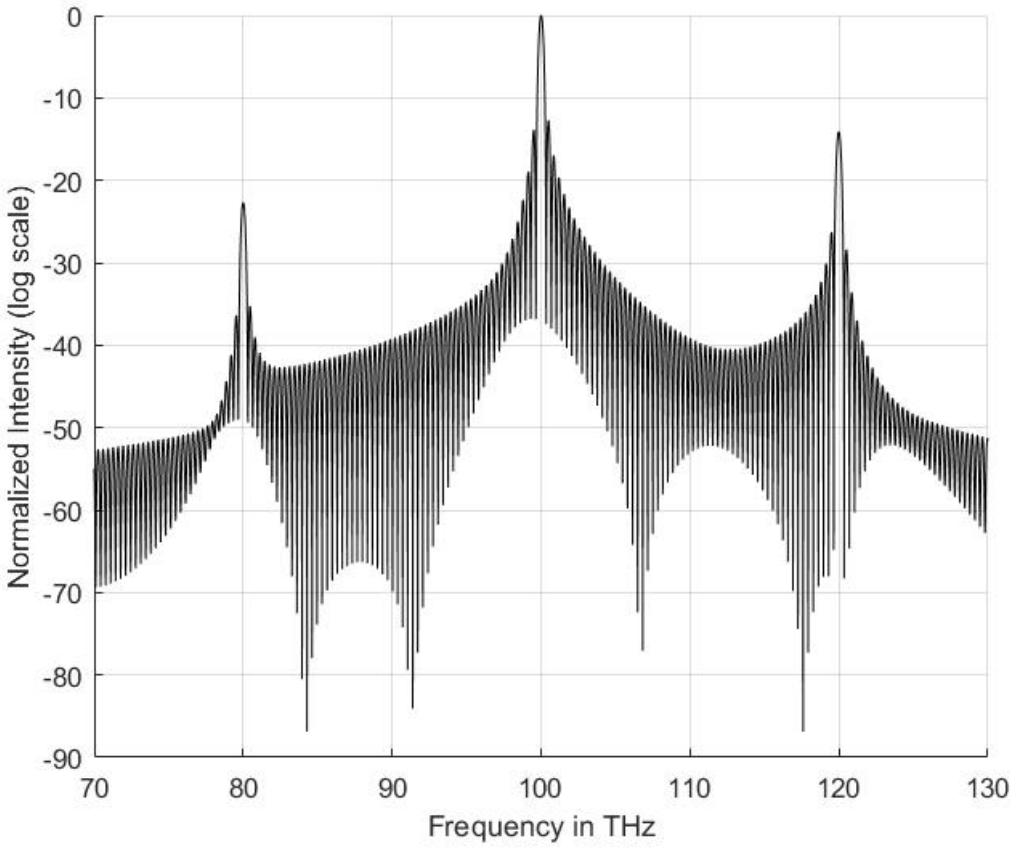

Figure 22. Spectrum of the Raman scattering observed with the incident frequency of 100Thz, and oscillation frequency set as 20THz, Stokes shift appeared at 80Thz and anti-Stokes at 120 THz.

5.2 Whispering-gallery Mode Resonance

Whispering-gallery mode (WGM) resonance occurs when an incident electromagnetic field becomes trapped near the inner surface of a structure due to total internal reflection. This process produces an evanescent electromagnetic field that results in an enhancement

of the local electric field intensity at certain “hot spots” near the surface. A few experimental studies have observed that WGM resonance can greatly enhance the intensity of Raman scattering [25, 26]. To better observe the enhancement effect by WGM resonance in an oscillating system, the following simulations are designed. Using the same schematic, we first locate the resonant frequencies of the structure by performing an initial simulation with a dipole Gaussian pulse excited next to the device without any oscillation. The wavelength injected by the source was set at 400nm, so it can comfortably cover the wavelength of visible light between 430nm to 770nm. An observation point was set right next to the device to capture the fields trapped near the surface. The resonant frequencies of the structure can be found by taking the Fourier transform of the field at the observation point over time. After choosing a resonance to study, multiple simulations were conducted with different incident frequencies that cover the resonance peak and observe the responses of the Raman scattering intensity.

5.3 Raman Shift near WGM Resonance

A different set of parameters for the device was chosen to further test our model, the configuration has a 1 micrometer diameter and a permittivity of 2.25. The stationary WGM resonances of this device are shown in Figure.9, the second resonance was chosen since a significant portion of the first resonance peak is outside the wavelength range of visible light. However, the resonances will be changed during the oscillation since deformation will slightly affect the optical property of the device. The exact resonance change cannot be directly predicted, but the range of resonance could be roughly estimated.

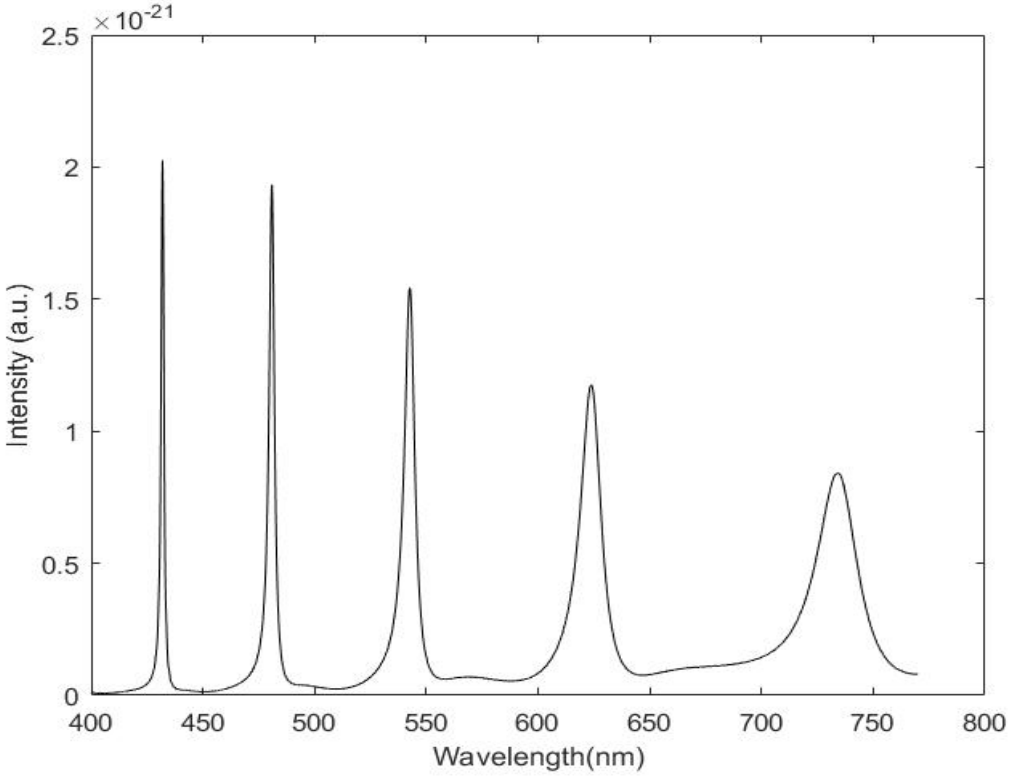

Figure 9. Spectrum of electric field resonance of the structure obtained with a dipole excitation, the WGM resonance wavelengths are around 431.93nm, 480.8nm, 542.6nm, 623.8nm, 734nm.

Recall that the device previously designed has three ultimate forms, an equilibrium circle, an ellipse expands in x direction and contract in y direction in between the first and second quarter periods formulated by the first equation in Eq. (4.6), another ellipse deformed in the opposite direction between the third and last quarter periods formulated by the second equation in Eq. (4.6). Using the same procedure mentioned previously, the stationary WGM resonances of the device in its ellipse forms can also be obtained. Figure.10 shows these three resonances around the same wavelength peak selected earlier. The resonance wavelength of the equilibrium is round 480.9nm, the ellipse expands in x direction have a resonance shifted round 481.25nm, and the ellipse expands in y direction have a resonance shifted to 481.35nm. The overall shape of the resonance curves is roughly

the same, and the shift of the resonance wavelength is minuscule compared to the overall coverage of the peaks.

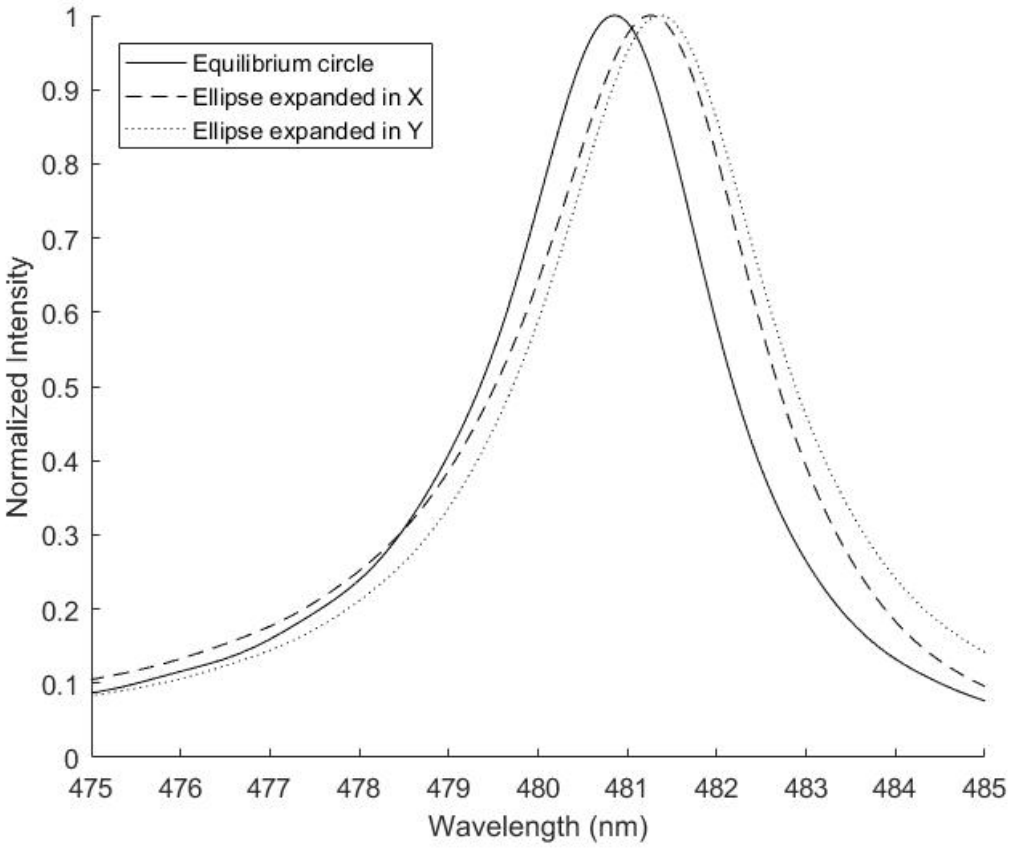

Figure 10. Spectrum of the device in three different deformed states, solid line is the equilibrium in both Eq. (4.7) and Eq. (4.10) which resonate at around 480.9nm the dashed line is the described by Eq. (4.9) have a resonance at round 481.25nm, the dotted line represents the resonance described by Eq. (4.11) have a resonance around 481.35nm

The real resonance of the oscillating device should be somewhere in between the equilibrium resonance at 480.9nm and its furthest shift at 481.35nm. To investigate this, multiple simulations were run at different incident wavelengths between 476nm and 484nm with an increment of 1nm below the half maximum of the equilibrium resonance peak and a finer increment of 0.5nm during 479.5nm - 480.5nm and 481.5nm - 482.5nm, then the smallest increment of 0.1nm between 480.5nm and 481.5nm. By doing this we not only are able to cover the majority of the resonance in order to observe the enhancement effect

but also have a better resolution at the top to locate the shifted resonance. The oscillation frequency was chosen to be 15 terahertz to ensure that the Raman shift would not inadvertently interact with any resonance and reside in frequencies that are relatively steady in-between resonances. Therefore, the responses from the field were only caused by the differences in incident frequency.

The results of our FDTD simulations are shown in Figure.11, comparisons have been made between the normalized Raman shift intensity and two WGM resonances mentioned previously, the equilibrium circle and the maximum ellipse expands in y direction. As we can observe, the response of the Raman shift intensity is greatly enhanced when incident wavelengths are near the resonance, the enhancement also approximately follows the trajectory of the WGM resonance curve. The Raman shift intensity peaked at 481.1nm

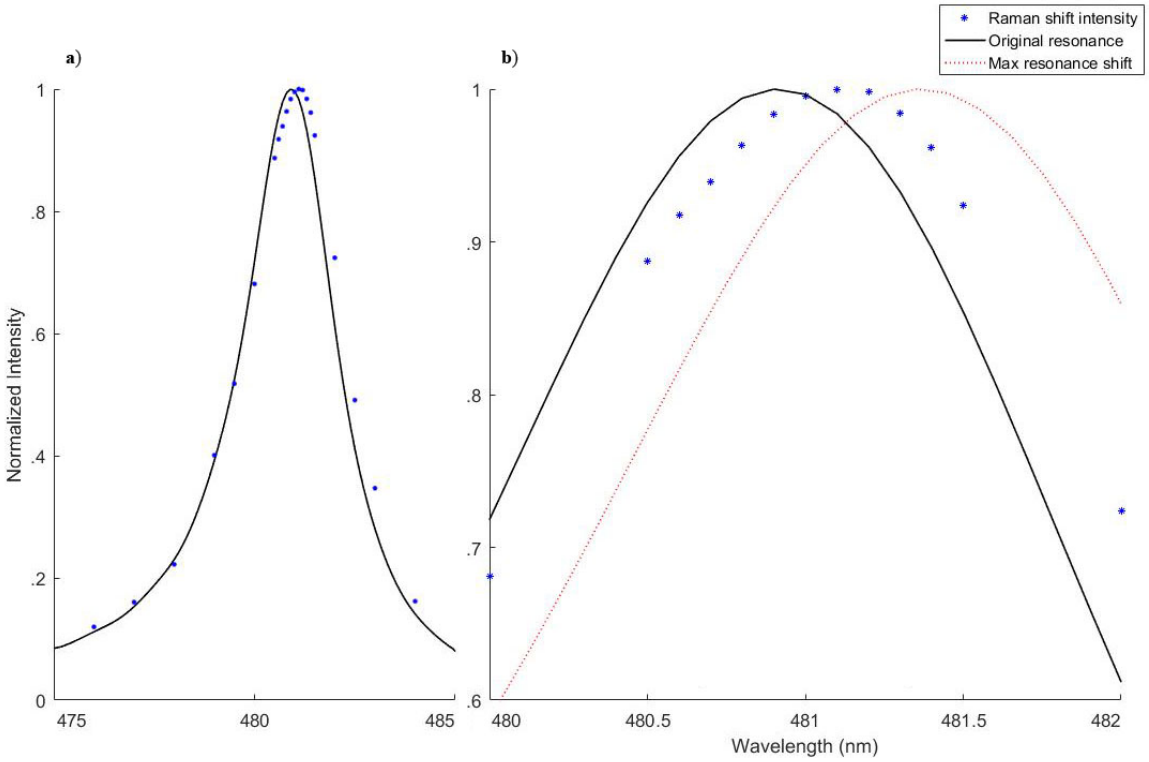

Figure 11. a) Overall spectrum of the Raman shift intensity obtained by multiple simulations compared to the resonance of the device in equilibrium position. b) Visualization of the shift of resonance in detail, the Raman shift intensity peaked at 481.1nm compared to the resonance in equilibrium position at 480.9nm and the maximum possible resonance shift at 481.35nm.

which indicate the oscillatory motion causes the WGM resonance shifted to around 481.1nm as predicted between 480.9nm and 481.35nm. However, this shift is so tiny and unnoticeable that can be easily overlooked. The Raman shift intensity at the original resonance peak position of 480.9nm still has over 98% of the enhancement compared to the maximum value at 481.1nm. One can easily perceive 480.9nm as the resonance peak if they are not deliberately looking for this shift.

6. Conclusions and Future Work

This project studied the problem of using the finite difference time domain method to simulate the electromagnetic response of oscillating structures. An algorithm was proposed and implemented to model a two-dimensional cylindrical rod with microscopic oscillation to explore the scattering of electromagnetic waves. The boundaryh of the oscillating device was addressed with a transitional permittivity variation between displacements. This implementation was verified through simulations and observation of the Raman effect occurs when electromagnetic wave scattering from an oscillating object.

In Section 5.1, the sidebands of Raman effect were successfully observed and both Stokes frequency shift and anti-Stokes frequency shift are within the expectations of Raman effect. Then in Section 5.3, by running multiple simulations with gradually increasing incident wavelengths, the Raman scattering enhancement effect was further explored, that is when the incident wave is close to Whispering-gallery mode resonances which are inherent in a cylindrical device. As observed, the enhancement roughly follows the trajectory of the WGM resonance curve. In addition, a resonance shift caused by the oscillatory motion of the device was predicted to have a wavelength between the resonance of the device in its equilibrium form and the resonance of the device with maximum deformation. This shift, which is tiny and can be easily neglected was also successfully observed.

Hopefully, the work performed in this project provides a basis for future understanding of interactions between dynamic objects and electromagnetic waves. However, there are still many issues need to be further studied. Such as, it would be interesting to know how the shift in resonance will be affected by changing the properties of the oscillation such as the amplitude or frequency, and how will the field react to materials other than dielectrics. The program implemented in this project can be extended into three dimensions, and more

complex form of vibration or oscillation can be implemented and studied. At last, instead of forcing the device to oscillate, we can integrate Newtonian dynamics into the system and model oscillations excited by electromagnetic waves.

References

[1] Bethune-Waddell, M., & Chau, K. J. (2015). Simulations of radiation pressure experiments narrow down the energy and momentum of light in matter. *Reports on Progress in Physics*, *78*(12), 122401.
[2] Mihiretie, B. M., Snabre, P., Loudet, J. C., & Pouligny, B. (2014). Optically driven oscillations of ellipsoidal particles. Part I: Experimental observations. The European Physical Journal E, 37(12), 124.
[3] Loudet, J. C., Mihiretie, B. M., & Pouligny, B. (2014). Optically driven oscillations of ellipsoidal particles. Part II: Ray-optics calculations. *The European Physical Journal E*, *37*(12), 125.
[4] Taylor, C., Lam, D. H., & Shumpert, T. (1969). Electromagnetic pulse scattering in time-varying inhomogeneous media. *IEEE Transactions on Antennas and Propagation*, *17*(5), 585-589.
[5] Harfoush, F. A., & Taflove, A. (1991). Scattering of electromagnetic waves by a material half-space with a time-varying conductivity. *IEEE Transactions on Antennas and Propagation*, *39*(7), 898-906.
[6] Liu, X., & McNamara, D. A. (2007). The use of the FDTD method for electromagnetic analysis in the presence of indepedently time-varying media. *International Journal of Infrared and Millimeter Waves*, *28*(9), 759-778.
[7] Harfoush, F., Taflove, A., & Kriegsmann, G. A. (1989). A numerical technique for analyzing electromagnetic wave scattering from moving surfaces in one and two dimensions. *IEEE Transactions on Antennas and Propagation*, *37*(1), 55-63.
[8] Inman, M. J., Elsherbeni, A. Z., & Smith, C. E. (2003, May). Finite difference time domain simulation of moving objects. In *Radar Conference, 2003. Proceedings of the 2003 IEEE* (pp. 439-445). IEEE.
[9] Iwamatsu, H., & Kuroda, M. (2010, July). Computational algorithm of FDTD method for the Lorentz transformation. In *Antennas and Propagation Society International Symposium (APSURSI), 2010 IEEE* (pp. 1-4). IEEE.
[10] Murray, D. B., Netting, C. H., Mercer, R. D., & Saviot, L. (2007). Polarizability calculation of vibrating nanoparticles for intensity of low wavenumber Raman scattering. *Journal of Raman Spectroscopy*, *38*(6), 770-779.
[11] Ahmed, A., Pelton, M., & Guest, J. R. (2017). Understanding How Acoustic Vibrations Modulate the Optical Response of Plasmonic Metal Nanoparticles. *ACS nano*, *11*(9), 9360-9369.
[12] Eichenfield, M., Chan, J., Camacho, R. M., Vahala, K. J., & Painter, O. (2009). Optomechanical crystals. *Nature*, *462*(7269), 78-82.
[13] Johnson, S. G., Ibanescu, M., Skorobogatiy, M. A., Weisberg, O., Joannopoulos, J. D., & Fink, Y. (2002). Perturbation theory for Maxwell's equations with shifting material boundaries. *Physical review E*, *65*(6), 066611.
[14] Yee, K. (1966). Numerical solution of initial boundary value problems involving Maxwell's equations in isotropic media. *IEEE Transactions on antennas and propagation*, *14*(3), 302-307.
[15] Taflove, A., & Hagness, S. C. (2000). Computational Electrodynamics: the FDTD method. *Artech House Boston, London*.
[16] Berenger, J. P. (1994). A perfectly matched layer for the absorption of electromagnetic waves. *Journal of computational physics*, *114*(2), 185-200.
[17] Gedney, S. D. (1996). An anisotropic perfectly matched layer-absorbing medium for the truncation of FDTD lattices. *IEEE transactions on Antennas and Propagation*, *44*(12), 1630-1639.
[18] Sacks, Z. S., Kingsland, D. M., Lee, R., & Lee, J. F. (1995). A perfectly matched anisotropic absorber for use as an absorbing boundary condition. *IEEE transactions on Antennas and Propagation*, *43*(12), 1460-1463.
[19] Hasegawa, T., Umemura, J., & Takenaka, T. (1993). Simple refraction law for uniaxial anisotropic absorbing media. *Applied spectroscopy*, *47*(3), 338-340.
[20] Whittaker, E. T. (1903). On the partial differential equations of mathematical physics. *Mathematische Annalen*, *57*(3), 333-355.
[21] Merewether, D. E., Fisher, R., & Smith, F. W. (1980). On implementing a numeric Huygen's source scheme in a finite difference program to illuminate scattering bodies. *IEEE Transactions on Nuclear Science*, *27*(6), 1829-1833.
[22] Raman, C. V. (1928). A new radiation. *Indian J. Phys*. **2**: 387–398.
[23] Long, D. A. (2002). The Raman effect: a unified treatment of the theory of Raman scattering by molecules. *West Sussex*.
[24] Fante, R. (1971). Transmission of electromagnetic waves into time-varying media. *IEEE Transactions on Antennas and Propagation*, *19*(3), 417-424.s

[25] Snow, J. B., Qian, S. X., & Chang, R. K. (1985). Stimulated Raman scattering from individual water and ethanol droplets at morphology-dependent resonances. Optics Letters, 10(1), 37-39.
[26] Symes, R., Sayer, R. M., & Reid, J. P. (2004). Cavity enhanced droplet spectroscopy: Principles, perspectives and prospects. Physical Chemistry Chemical Physics, 6(3), 474-487.

Appendix

The FDTD code developed during the project will be documented in this section. Comments will be provided to explain the meaning of different variables in the context of our FDTD formulation. A portion of the code will be omitted since they are not essential to the formulation, such as define the common units, coefficients, parameter of the problem domain, collecting field data and visualization etc.

1. Pre-loop Computation

```
%%Source configuration
This section defines the extraction source function described in section 3.8. Ez_src is the final product contain the field information of the source at any time during the simulation. t_prop is the time it would take for wave travel through the problem domain. STEPS is the total timesteps before the simulation ends. freq is the incident frequency. tw is the halfwidth of the Gaussian pulse, t0 is the temporal delay described in Eq.(3.61). Gt is the smoothing function defined as half of a normal Gaussian function described in Eq.(3.62)

%%Gaussian source
tw = 0.5/freq;
t0 = 5*tw;
t_prop = dy*Ny/c0;
STEPS  = ceil((2*t0+20*t_prop)/dt);
t_max  = (0:STEPS-1)*dt;
Ez_src = exp(-((t_max-t0)/tw).^2);

% Sinusoidal source
t0=(4*3+1)/4/freq;
tw=t0/3;
ta=(0:STEPS-1)*dt;
Gt=exp(-((ta-t0)/tw).^2);
t1=round(t0/dt);
Gt(t1:end)=1;
t_prop=dy*Ny/c0/dt;
STEPS  = ceil((2*t0+100*t_prop)/dt);
t_max  = (0:STEPS-1)*dt;
Ez_src = Gt(T)*sin(2*pi*freq* t_max  *dt);

%%PML coefficient configuration
This section defines coefficients of the perfectly matched layer described in section 3.5 and 3.6, a 2-x grid technique is used to provide a smoother result. Nx,Ny define the size of our problem domain. Sigmax and sigx,sigy correspond to σ_max .  and σ_x,y,z .  in Eq.(3.32). PML_size() was defined as the length of the PML in four directions.
Nx2 = 2*Nx;
Ny2 = 2*Ny;
sigmax=4/150/pi/dx;
sigx = zeros(Nx2,Ny2);
sigy = zeros(Nx2,Ny2);
x = 1 : 2*PML_size(1)
```

```
nx = 2*PML_size(1) - x + 1;
sigx(nx,:) = (sigmax)*(x/2/PML_size(1))^3;
end
for x = 1 : 2*PML_size(2)
nx = Nx2 - 2*PML_size(2) + x;
sigx(nx,:) = (sigmax)*(x/2/PML_size(2))^3;
end
for y = 1 : 2*PML_size(3)
ny = 2*PML_size(3) - y + 1;
sigy(:,ny) = (sigmax)*(y/2/PML_size(3))^3;
end
for y = 1 : 2*PML_size(4)
ny = Ny2 - 2*PML_size(4) + y;
sigy(:,ny) = (sigmax)*(y/2/PML_size(4))^3;
end

% Compute update coefficient for updating Hx, Hy,Ez in Eq.(3.56-3.58)
sigHx = sigx(1:2:Nx2,2:2:Ny2);
sigHy = sigy(1:2:Nx2,2:2:Ny2);
mHx0 = (1/dt) + sigHy/(2*e0);
mHx1 = ((1/dt) - sigHy/(2*e0))./mHx0;
mHx2 = c0./URxx./mHx0;
mHx3 = (c0*dt/e0) * sigHx./URxx ./ mHx0;
%HY
sigHx = sigx(2:2:Nx2,1:2:Ny2);
sigHy = sigy(2:2:Nx2,1:2:Ny2);
mHy0 = (1/dt) + sigHx/(2*e0);
mHy1 = ((1/dt) - sigHx/(2*e0))./mHy0;
mHy2 = c0./URyy./mHy0;
mHy3 = (c0*dt/e0) * sigHy./URyy ./ mHy0;
%EZ
sigEx = sigx(1:2:Nx2,1:2:Ny2);
sigEy = sigy(1:2:Nx2,1:2:Ny2);
mEz1 = (sigEx + sigEy)/(2*e0) + sigEx.*sigEy*(dt/4/e0^2);
mEz2 = (dt/e0^2)*sigDx.*sigDy;
```

2. FDTD Loop

This section contains the update equations for our FDTD simulation, the process is in a

loop that will end when the maximum time-steps STEP is reached.

```
for T = 1:STEPS
%ERzz and SGzz is the Time-varying permittivity and conductivity matrix
described in Eq. (4.12). ERzz_1 and ERzz_1 store the permittivity and
conductivity from previous timestep used in Eq. (3.58). Oscillation()is
the implementation of our oscillatory motion which will be expanded in
next section. Ez_inc is the Ez component of our secondary grid that was
required to calculate correction terms for our TF/SF formulation in
section 3.10, any field component with a postfix of "_inc" is the
component of the secondary grid. The secondary field are updated alongside
with the main grid.
      ERzz_1 = ERzz;
      SGzz_1 = SGzz;
```

```
      [ERzz,OBJ,SGzz]=
      Oscillation(Nx,Ny,T,o_period,radius,o_amplitude,x0,y0,er1,er2);
      Ez_inc(y_src-1) = Ez_src;
%Spatial approximation to update the curl of E in x direction CEx for
all grids in problem domain using Eq.(3.18)
      for y = 1 : Ny-1
            for x = 1 : Nx
                  CEx(x,y) = (Ez(x,y+1) - Ez(x,y))/dy;
            end
            CEx_inc(y) = (Ez_inc(y+1) - Ez_inc(y))/dy;
      end
      for x = 1 : Nx
            CEx(x,Ny) = (Ez(x,1) - Ez(x,Ny))/dy;
      end
      CEx_inc(Ny) = - Ez_inc(Ny)/dy;
%Spatial approximation to update the curl of E in y direction CEy
across the grids in problem domain using Eq.(3.19)
      for x = 1 : Nx-1
            for y = 1 : Ny
                  CEy(x,y) = - (Ez(x+1,y) - Ez(x,y))/dx;
            end
      end
      for y = 1 : Ny
            CEy(Nx,y) = - (Ez(1,y) - Ez(Nx,y))/dx;
      end
%Correction for CEx and CEy on the TF/SF boundary described in
Eq.(3.67,3.69,3.73,3.75).
      CEx(x_src,y_src)=CEx(x_src,y_src)- Ez_inc(y_src)/dy;
      CEx(x_src,P_incD)=CEx(x_src, P_incD)+ Ez_inc(P_incD+1)/dy;
      for y = y_src+1 : P_incD
            CEy(P_incL-1,y) = CEy(P_incL-1,y) + Ez_inc(y)/dx;
            CEy(P_incR,y) = CEy(P_incR,y) - Ez_inc(y)/dx;
      end

%Update the Integration Terms SumCEx, SumCEy, SumCEx_inc for curl of E
that is needed in for updating Hx and Hy.
      SumCEx = SumCEx + CEx;
      SumCEy = SumCEy + CEy;
      SumCEx_inc = SumCEx_inc + CEx_inc;
%Temporal approximations to update Hx and Hy using update equations in
Eq.(3.56-3.57)
      Hx = mHx1.*Hx - mHx2.*CEx - mHx3.*SumCEx;
      Hy = mHy1.*Hy - mHy2.*CEy - mHy3.*SumCEy;
      Hx_inc = mHx1(P_incL,:).*Hx_inc - mHx2(P_incL,:).*CEx_inc -
      mHx3(P_incL,:).*SumCEx_inc;
%Spatial approximation to update the curl of H in z direction CHz for
grids in problem domain using Eq.(3.20)
      CHz(1,1) = (Hy(1,1) - Hy(Nx,1))/dx - (Hx(1,1) - Hx(1,Ny))/dy;
      CHz_inc(1) =-(Hx_inc(1) - Hx_inc(Ny))/dy;
      for x = 2 : Nx
            CHz(x,1) = (Hy(x,1) - Hy(x-1,1))/dx - (Hx(x,1) -
            Hx(x,Ny))/dy;
      end
      for y = 2 : Ny
            CHz(1,y) = (Hy(1,y) - Hy(Nx,y))/dx - (Hx(1,y) - Hx(1,y-
      1))/dy;
            CHz_inc(y) =-(Hx_inc(y) - Hx_inc(y-1))/dy;
```

```
            for x = 2 : Nx
                  CHz(x,y) = (Hy(x,y) - Hy(x-1,y))/dx - (Hx(x,y) -
            Hx(x,y-1))/dy;
            end
      end
%Correction for CHz on the TF/SF boundary described in
Eq.(3.68,3.70,3.72,3.74).
      CHz(x_src,y_src) = CHz(x_src,y_src) + Hx_inc(y_src)/dy;
      CHz(x_src,P_incD+1) = CHz(x_src,P_incD+1) - Hx_inc(P_incD)/dy;
%Temporal approximations to update Ez using update equations in
Eq.(3.58)
      ERzz_1=ERzz_1/2+ERzz/2;
      SGzz_1=SGzz_1/2+SGzz/2;
      Ez = (ERzz_1/dt-SGzz_1/e0-mEz1).*Ez + c0.*CHz - mEz2.*SumEz;
      Ez = Ez./(ERzz1/dt+SGzz_1/e0+mEz1);
      Ez_inc = (ERzz_1(P_incL,:)./dt-SGzz_1(P_incL,:)/e0-
      mEz1(P_incL,:)).*Ez_inc + c0.*CHz_inc-mEz2(P_incL,:).*SumEz_inc;
      Ez_inc =
      Ez_inc./(ERzz1(P_incL,:)/dt+SGzz_1(P_incL,:)/e0+mEz1(P_incL,:));
end
```

3. Oscillation Function

This section presents the implementation of the oscillation function described in Section 4.2 and 4.3.

```
%The function receives the parameters Nx Ny which is the size of the grid,
timestep T, oscillation period p, radius r, oscillation displacement d,
the center position of device (x0,y0), relative permittivity of
surrounding media er1, relative permittivity of the device er2 and the
conductivity of the device sg. Then output the permittivity and
conductivity matrices of the device ERzz and SGzz at given timestep. A
third matrix OBJ which correspond to O(t) in Eq.(4.7-4.11) is also
returned to the main program, but it is only used for visualization
purpose. a and b correspond to the major and minor axis of the ellipse,d_ab
correspond to Δd in ellipse formulations and dp correspond to p/4d_max in
our transitional layer formulation.

function [ERzz,OBJ,SGzz]=Oscillation(Nx,Ny,T,p,r,d,x0,y0,er1,er2,sg)
      [y,x] = meshgrid(1:Ny,1:Nx);
      a=r+d;
      b=r-d;
      d_ab=d/p*4;
      dp=p/4/d;
      i=mod(T,p);
      if i<p/4
            j=mod(T,p/4);
            OBJ = sqrt(((x-x0).^2/(r+d_ab*j)^2) + ((y-y0).^2/(r-
            d_ab*j)^2))<1;
            OBJ_1 = sqrt(((x-x0).^2/(r+d_ab*j+1)^2) + ((y-y0).^2/(r-
            d_ab*j-1)^2))<1;
      elseif i<p/2
            j=mod(T,p/4);
```

```
            OBJ = sqrt(((x-x0).^2/(a-d_ab*j)^2) + ((y-
            y0).^2/(b+d_ab*j)^2))<=1;
            OBJ_1 = sqrt(((x-x0).^2/(a-d_ab*j-1)^2) + ((y-
            y0).^2/(b+d_ab*j+1)^2))<1;
      elseif i<3*p/4
            j=mod(T,p/4);
            OBJ = sqrt(((x-x0).^2/(r-d_ab*j)^2) + ((y-
            y0).^2/(r+d_ab*j)^2))<1;
            OBJ_1 = sqrt(((x-x0).^2/(r-d_ab*j-1)^2) + ((y-
            y0).^2/(r+d_ab*j+1)^2))<1;
      else
            j=mod(T,p/4);
            OBJ = sqrt(((x-x0).^2/(b+d_ab*j)^2) + ((y-y0).^2/(a-
            d_ab*j)^2))<1;
            OBJ_1 = sqrt(((x-x0).^2/(b+d_ab*j+1)^2) + ((y-y0).^2/(a-
            d_ab*j-1)^2))<1;
      end
      OBJ =1.*OBJ;
      OBJ_1=1.*OBJ_1;
      SGzz = OBJ.*sg;
      ERzz = (er2-er1).*OBJ+er1;
end
```